Master's thesis

Odd-Einar C. Nervik

Cosmic Ray Diffusion in the Hamiltonian Guiding Center Approximation

NTNU
Norwegian University of Science and Technology
Faculty of Natural Sciences
Department of Physics

NTNU
Norwegian University of
Science and Technology

Odd-Einar Cedervall Nervik

Cosmic Ray Diffusion in the Hamiltonian Guiding Center Approximation

Master's thesis in Applied Physics and Mathematics
Supervisor: Prof. Michael Kachelrieß
June 2019

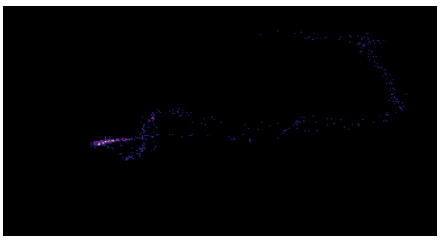

NTNU
Norwegian University of
Science and Technology

Odd-Einar Cedervall Nervik

Cosmic Ray Diffusion in the Hamiltonian Guiding Center Approximation

Master's thesis in Applied Physics and Mathematics
Supervisor: Prof. Michael Kachelrieß
June 2019

Norwegian University of Science and Technology
Faculty of Natural Sciences
Department of Physics

NTNU
Norwegian University of
Science and Technology

Abstract

To provide a method of testing the accuracy of the Hamiltonian Guiding Center Approximation, the diffusion coefficients of cosmic rays propagating in a purely turbulent magnetic field is investigated. The goal is to reproduce earlier results to assure the diffusion simulations can be used to compare the Hamiltonian guiding center theory to the direct solving of the Lorentz-equation. The turbulence is simulated as a hydrodynamic turbulence following the Kolmogorov power spectrum. To simulate the cosmic ray propagation a step-size controlled Runge-Kutta algorithm is implemented to solve the Lorentz-equation. The isotropy of the algorithm generating the turbulent magnetic field is verified, and isotropy is proven given the correct choice of probability distribution for the random phases. Furthermore, the qualitative behavior of the diffusion coefficients is shown to be in accordance with previous results in both the isotropic and anisotropic regimes. After transitioning to the isotropic regime the factor d_3/d_1 is found to be constant at $d_3/d_1 \sim 10$, which shows a significant amount of anisotropic behavior. Comparing the amplitude of the average diffusion coefficients from the simulations with theoretical coefficients show that they are within a factor of 1.21 and 2.33. The scaling of the diffusion coefficient is found to follow the expected $D(E) \propto \beta$ when $\beta = 1/3$ and $\beta = 2$ for the diffusive and ballistic regimes respectively. The transition is shown to begin at a slightly higher energy for the simulated diffusion than for the theoretical diffusion.

Hamiltonian guiding center theory is applied to the propagation of cosmic rays through different magnetic field models, including the uniform field, spiral fields with constant and non-constant field strengths, and a uniform field in superposition with a turbulent field. The aim is to test under which conditions the Hamiltonian guiding center theory can replace the direct solution of the Lorentz-equation and still provide equal results. Furthermore it is tested whether the guiding center theory is able to increase the efficiency of these simulations.

It is shown that guiding center theory accurately reproduces the equivalent trajectory to that of the direct solution of the Lorentz-equation, exempt of a drift velocity caused by the curl of the magnetic field and an acceleration caused by the gradient of the magnetic field strength. The exemption of these effects are shown to be missing due to errors in the implementation. The presented results suggest that the Hamiltonian guiding center theory, when implemented correctly, will be able to accurately simulate the trajectories of cosmic rays through a Galactic magnetic field. The simulations using the guiding center theory also suggest the theory will be more efficient than directly solving the Lorentz-equation.

As the guiding center theory implementation was not completed within the time frame of this project, it was not possible to implement it in the simulation of diffusion of cosmic rays in the Galactic magnetic field.

Sammendrag

For å konstruere en metode til å teste nøyaktigheten til den Hamiltonske føringssenterapproksimasjonen undersøkes diffusjonskoeffisientene av kosmiske stråler propagert i et turbulent magnetisk felt. Målet er å reprodusere tidligere resultater for å forsikre at diffusjonssimuleringene kan benyttes til å sammenligne den Hamiltonske føringssenterapproksimasjonen opp mot det å løse Lorentz-ligningen direkte. Turbulensen simuleres som en hydrodynamisk turbulens som følger Kolmogorov's energispektrum. For å simulere propagasjonen av kosmisk stråling ble en Runge-Kutta-integrator implementert for å løse Lorentz-ligningen. Isotropien av algoritmen som genererer det turbulente magnetfeltet verifiseres, og isotropien i feltet bevises gitt at korrekt sannsynlighetsfordeling for de tilfeldige fasene velges. Videre vises den kvalitative atferden av diffsjonskoeffisientene å være i samsvar med tidligere resultater. Etter overgangen til det isotropiske regime finnes faktoren d_3/d_1 til å være tilnærmet konstant ved $d_3/d_1 \sim 10$, som viser en signifikant anisotropisk atferd. Sammenligning av de gjennomsnittlige diffusjonskoeffisientene fra simuleringene opp mot de teoretiske verdiene viser at forskjellen er innen en faktor mellom 1.21 og 2.33. Diffusjonskoeffisienten vises å følge $D(E) \propto \beta$ som forventet, med $\beta = 1/3$ og $\beta = 2$ for the diffusive og det ballistiske regime respektivt. Videre vises det at overgangen mellom de to regimene starter ved høyere energi for de simulerte diffusjonskoeffisientene enn for de teoretiske koeffisientene.

Hamiltonsk føringssenterteori anvendes på propageringen av kosmisk stråling gjennom forskjellige magnetiske felt, inklusive det uniforme feltet, spiralfelt med konstant og varierende feltstyrke, samt et uniformt felt i superposisjon med et turbulent felt. Målet er å teste under hvilke forhold føringssenterteorien kan brukes i stedet for å løse Lorentz-ligningen direkte, og fortsatt gi ekvivalente resultater. Videre testes det om føringssenterteorien øker effektiviteten i disse simuleringene.

Det vises at føringssenterteorien reproduserer en tilsvarende bane til den produsert av den eksakte løsningen, med unntak av drifteffekter påført av curlen til magnetfeltet, samt en akselerasjonseffekt påført av magnetfeltets gradient. Disse manglende effektene vises å komme av en feil i programmeringen av teorien. Resultatene peker mot at Hamiltonsk føringssenterteori, når den implementeres korrekt, vil simulere banene til kosmisk stråling gjennom det Galaktiske magnetfeltet med høy nøyaktighet. Simuleringene antyder også at føringssenterteorien vil være mer effektiv enn å løse Lorentz-ligningen direkte.

Siden implementasjonen av føringssenterteorien ikke ble ferdigstilt inne tidsrammen av dette prosjektet, var det ikke mulig å implementere den i beregningene av diffusjonen av kosmisk stråling i det galaktiske magnetiske feltet.

Preface

The presented thesis is the culmination of my Master's project, and concludes my degree as Master of Science in Applied Physics and Mathematics. The thesis is worth 30 ECTS and is written at the Norwegian University of Science and Technology, NTNU, Trondheim. The project is done under the supervision of Prof. Michael Kachelrieß at the Department of Physics.

With this I thank Prof. Michael Kachelrieß for his guidance throughout both the Master's project and the project assignment. The projects have been challenging, interesting and provided substantial learning. I would not have made the progress I did if it was not for the continued guidance and support of Prof. Kachelrieß.

I would like to thank the people who helped me correct and proof read the thesis: Gry Emilie, Douwe and Markus. The help they have provided has been indispensable.

Lastly I thank Birk and Markus for their company during these two projects. The late nights at 'Fysikkland' would not have been the same without them.

Trondheim, 2019-06-25

Odd-Einar Cedervall Nervik

CONTENTS

LIST OF TABLES

LIST OF FIGURES

CHAPTER 1

INTRODUCTION

Background

"In the Milky Way, the Galactic magnetic fields affect all phases of the interstellar medium from the propagation of relativistic cosmic rays to the collapse of cold dust clouds." (Boulanger et al., 2018)

Throughout the Milky Way a magnetic field has been observed, roughly following the spiral structure of the galaxy. The first observations of a magnetic field outside of Earth were done in 1908. These observations were done by direct measurement of the Zeeman effect in the magnetic fields in sunspots. 42 years later it was suggested that magnetic fields were required for the creation, as well as the containment of Cosmic Rays (CR) within the Galaxy. The synchroton emission theory was developed, leading to the suggestion that relativistic CRs should be highly polarized. In 1954 the first observations of highly polarized optical radiation were performed by observing the Crab Nebula. The results were later confirmed in 1957. A few years later, in 1962, the detection of Faraday rotation in extragalactic CRs was confirmed by observing Centaurus A. It soon followed that the interstellar medium in the Milky Way could also cause Faraday rotation. Development of these methods for observing magnetic fields in the interstellar and extragalactic media finally led to the collection of data on the structure of the Galactic magnetic field in the Milky Way from 1968 and onward. (Beck, 2003; Beck and Wielebinski, 2013; Boulanger et al., 2018)

The magnetic field in the Milky Way can be considered as a superposition of a large-scale field and small-scale field (Haverkorn, 2014), where the large-scale field is a coherent component (also referred to as the regular component) which roughly follows the spiral arms of the Galaxy. The strength of this coherent magnetic

Figure 1.1: A picture of the spiral galaxy M-51 overlaid with the magnetic field vectors (yellow) and contours of the radio emission. The picture was taken by the Hubble Space Telescope. (Picture used with permission from MPIfR Bonn. Copyright: MPIfR Bonn and NASA/ESA (Hubble Heritage Team). Graphics: Sterne und Weltraum.)

field has been derived from Faraday rotation measurements to $\sim 2\,\mu G$ (Boulanger et al., 2018). The small-scale structures are caused by a range of phenomena, e.g. supernova explosions and shock wave remnants among others (Haverkorn, 2014). These small-scale fields, also called turbulent fields, are approximated by a power law given with a certain coherence length. Studies suggest coherence lengths of $\sim$ a few to 200 pc within the spiral arms of the Galaxy (Giacinti et al., 2012). Even though these small-scale fields contribute a random turbulence, the Root Mean Square (RMS) value of the turbulent field has been measured to $\sim 3 - 5\,\mu G$ in the spiral (Beck and Wielebinski, 2013). The total field strength in the solar neighbourhood has been derived from synchrotron measurements, and has been found to be $\sim 6\,\mu G$ (Beck, 2003; Boulanger et al., 2018). At the galacto-centric radius of 3 kpc the estimates of this value increases to ranges from $\sim 10\,\mu G$ to $\sim 1\,mG$. Several estimates have been made for the magnetic field in the galactic center within this range, including the ranges $\sim 6 - 22\,\mu G$ and $\gtrsim 50 - 120\,\mu G$ (Haverkorn et al., 2015).

A vast range of phenomena on the galactic and extra-galactic scales observed throughout the universe, has been observed through Galactic CR originating from

the event causing the phenomenon. To accurately identify the sources of the Galactic CRs it is then important to understand how the Galactic magnetic field affects the propagation and diffusion of the Galactic CRs. As the Galactic magnetic field has a coherent part, the particles will gyrate about this coherent field with a Larmor radius proportional to the coherent field strength. At the same time the small-scale turbulent field will affect the propagation of the Galactic CRs. The effects of the turbulent field on the Galactic CRs is large enough to cause diffusion of the particles, which erases information about the sources from which they originated. A thorough understanding of how the particles diffuse due to the Galactic magnetic field will thus improve the ability to accurately identify the source of the Galactic CRs. Furthermore, the Galactic magnetic field produces Galactic polarized synchroton emission. This synchroton emission acts as a foreground for the cosmic microwave background polarization. Understanding the effects of the Galactic magnetic field on the polarization of the cosmic microwave background is thus of importance when studying the cosmic microwave background (Giacinti et al., 2012; Haverkorn, 2014).

To examine the interaction between particles and the Galactic magnetic field, different test-particle simulations have been used. By modelling the magnetic field as a coherent part in superposition with a turbulent field, these interaction can be simulated using well known numerical methods. In the case of the Galactic magnetic field it is usually assumed that there is no electric field, and so the simulations are done using numerical methods to solve the Newton-Lorentz equations. When solving these equations for a coherent field, the result is a helical trajectory about a magnetic field line. Adding the turbulent field, the helical movement is then dependent on the proportional strength between the coherent and the turbulent part. The computational cost when simulating a particle in this magnetic field increases with the relative strength of the turbulent field, and decreases when the energy of the test particle is increased. In itself a single particle trajectory is seldom of interest. Instead the diffusion of a multitude of particles, providing a statistical view of the Galactic magnetic field properties is what is of interest (Giacalone and Jokipii, 1994; Giacinti et al., 2012; Snodin et al., 2016). As such, the helical movement of each particle is disregardable, and only the motion of the Guiding Center (GC) is of actual interest. Simulating upwards of several hundred points, generating the computationally costly magnetic field at each of these points, just to get one period of helical motion then seems highly unnecessary. Implementing a method that only looks at the guiding center, and manages to incorporate the movement through both a coherent and turbulent field, would seemingly reduce the computational cost of each trajectory drastically.

Standard Guiding Center Theory (GCT) was developed by Northrop (1963). The theory faced several shortcomings, but it was not until GCT was combined

with numerical methods that these shortcomings became significant. Due to a lack of energy conservation, when applied to numerical analysis, errors accumulated as the simulations were run for longer periods of time. These shortcomings were eventually improved upon with the development of Hamiltonian GCT. Over the course of the next two decades, different methods were attempted to develop a Hamiltonian teory for the motion of the GC. Wong (1982) accomplished to formulate a canonical Hamiltonian GCT, but this theory required non-physical coordinates. Simultaneously Boozer (1980) showed that the GC Equations of Motion (EoM) could be derived from a Hamiltonian in curl-free magnetic fields. White et al. (1982) later showed that the same equations could be derived even when the magnetic field is not curl-free. During the same period, in a series of papers, Littlejohn derived his formulation of the GC phase-space Lagrangian through noncanonical Hamiltonian mechanics. The results of Littlejohn (1983) give the GC EoM in noncanonical coordinates, which are reviewed in Cary and Brizard (2009). The review by Cary and Brizard (2009) will be followed closely in this report, and the resulting EoM will be implemented numerically.

Intuitively it should save computational power to only simulate the motion of the GC compared to simulating the exact particle movement through the magnetic field. If the GCT proves to give the same statistical results as the exact solution of the Lorentz-equation, hereby known as the 'exact solution', while also significantly improve the simulation efficiency, this would allow for more thorough simulations of CRs in the complex Galactic magnetic field models.

Problem Formulation

In this report the following will be investigated:

1. The diffusion of Cosmic Rays through a purely TMF is to be simulated, using the turbulent magnetic field model from Giacalone and Jokipii (1994). The isotropy of the turbulent magnetic field is to be verified analytically, before the theory is used to verify the accuracy of the diffusion simulations. The final aim is to reproduce the results of Giacinti et al. (2012) and Giacinti et al. (2018), in order to assert the diffusion simulation as a method to compare the Hamiltonian GCT simulations to the exact simulations.

2. Hamiltonian GCT will be applied to the diffusion of Cosmic Rays in the Galactic Magnetic Field. By numerically propagating cosmic rays through different magnetic field models, the accuracy of the Hamiltonian GCT will be tested and compared to simulations of the exact solution solving the Lorentz-equation.

Objectives

This report aims to complete the objectives:

1. Implement a method to simulate cosmic ray propagation in a turbulent magnetic field, and verify the method by reproducing the results of Giacinti et al. (2012) and Giacinti et al. (2018).

2. Implement Hamiltonian GCT to the simulation of Cosmic Ray propagation in different magnetic field models, and verify that the new simulations reproduce the behavior of the exact solution.

3. Test the accuracy of the Hamiltonian GCT by simulating a significant amount of particles, using both the exact and guiding center methods, through a series of magnetic fields, and comparing the resulting trajectories.

4. Apply the Hamiltonian GCT to the diffusion of Cosmic Rays through a turbulent field, and test under which conditions the GCT can provide statistically accurate results.

5. For the conditions in which the Hamiltonian GCT proves to be accurate, test the efficiency of this method compared to the exact solution.

Structure of the Thesis

The thesis will be divided into two main parts, which are then linked together in the conclusion.

Chapters 2 and 3 will present the diffusion of Cosmic Rays in a turbulent field, using the exact solution. First Chapter 2 will present the needed theory, including the theory of how CRs propagate in magnetic fields, which effects a curl and a gradient in the magnetic field has on the trajectory of CRs, and how the diffusion tensor is calculated. Thereafter the implementation, results, and discussion of the results are presented in Chapter 3. This begins with a description of how trajectory simulations were programmed, and how the diffusion coefficients were calculated. After this the results are presented and discussed based on the expectations given by the theory and previous results.

The second main part consists of Chapters 4 and 5. The theory of the Hamiltonian guiding genter approximation is presented in Chapter 4, focusing on the derivation of the equations of motion. Following this, in Chapter 5, comes a detailed explanation of how the equations of motion was implemented as a program. Lastly, the results from the implementation of the GCT are presented and discussed on the basis of the theory and what is expected compared to the exact

solution. After the results are presented, there is a short section on known errors in the program, and suggestion on how the program can be developed further.

Finally Chapter 6 summarizes the findings of the thesis and draws the final conclusions.

CHAPTER 2

COSMIC RAY DIFFUSION IN TURBULENT MAGNETIC FIELDS

In this chapter the model of the turbulent magnetic field will be presented along with the theory of how CRs will propagate through such a field. Along with this the diffusion tensor and diffusion coefficients will be presented.

Turbulent Magnetic Fields

There are a number of ways to model turbulence in magnetic fields. One such model for the turbulence is a Gaussian random field with zero mean and a RMS value B_{rms}. As shown by Harari et al. (2002), this can be described as a superposition of Fourier modes on the form

$$B_i(\boldsymbol{x}) = \int \frac{d^3k}{(2\pi)^3} B_i(\boldsymbol{k}) e^{i(\boldsymbol{k}\cdot\boldsymbol{x}+\beta_i(\boldsymbol{k}))}, \tag{2.1.1}$$

where the phases $\beta_i(\boldsymbol{k})$ are a random, and $B_i(\boldsymbol{x})$ is the magnetic field component in the $\hat{\boldsymbol{e}}_i$-direction. The Fourier modes $\boldsymbol{k}$ are plane waves with a random direction. Following Maxwells equation $\nabla \cdot B = 0$, and inserting the magnetic field which is on the form $B(\boldsymbol{x}) \propto B(\boldsymbol{k})\boldsymbol{\zeta} e^{-i\boldsymbol{k}\cdot\boldsymbol{x}}$ (Giacinti et al., 2012), the constraint

$$\mathbf{B}(\boldsymbol{k}) \cdot \boldsymbol{k} = 0 \tag{2.1.2}$$

is found, where

$$\mathbf{B}(\boldsymbol{k}) = B_x(\boldsymbol{k})\hat{\boldsymbol{e}}_x + B_y(\boldsymbol{k})\hat{\boldsymbol{e}}_y + B_z(\boldsymbol{k})\hat{\boldsymbol{e}}_z\,. \tag{2.1.3}$$

For this field to be isotropic and homogeneous it has to satisfy

$$\langle \boldsymbol{B}(\boldsymbol{k}_i) \cdot \boldsymbol{B}^*(\boldsymbol{k}_j) \rangle = B^2(k)\delta_{ij} \tag{2.1.4}$$

where $|\boldsymbol{k}| = k$. By inserting Eq. (2.1.4) into the expectation of $\boldsymbol{B}(\boldsymbol{x})$, the RMS value can be defined as

$$B_{\text{rms}}^2 \equiv \langle \boldsymbol{B}(\boldsymbol{x}) \cdot \boldsymbol{B}^*(\boldsymbol{x}) \rangle = \int B^2(k) \mathrm{d}k \,. \tag{2.1.5}$$

Another model that fully characterizes turbulent magnetic fields is to model them as a power spetrum, following

$$E(L) \propto L^{\gamma} \tag{2.1.6}$$

where $E(L)$ is the energy of an eddie current with scale size L. γ is called the spectral index, and different models have different spectral indices. One model that fits well with observations of our Galaxy is the Kolmogorov spectrum, where $\gamma = 5/3$ (Giacinti et al., 2018). Since there is no electric field present in the Galactic magnetic field,

$$E(k) \propto B^2(k) \propto k^{-\gamma} \tag{2.1.7}$$

where it is used that $k = 2\pi/L$, with L being the wavelength of the Fourier modes modelling the magnetohydrodynamic eddies. By demanding the Fourier modes to be constrained by some values $k_{min} < k < k_{max}$ and inserting Eq. (2.1.7) into (2.1.5),

$$B^2(k) = B_{\text{rms}}^2 k^{-\gamma} \frac{(\gamma - 1) k_{\text{min}}^{\gamma - 1}}{1 - (k_{\text{min}}/k_{\text{max}})^{\gamma - 1}} \tag{2.1.8}$$

gives the magnetic field strength for each mode k.

Correlation length

To understand how the turbulent magnetic field varies within the constraint $L_{\text{min}} < L < L_{\text{max}}$, it is of interest to find the correlation length. Harari et al. (2002) defines this as

$$L_c B_{\text{rms}}^2 \equiv \int_{-\infty}^{\infty} \mathrm{d}L \langle \, \boldsymbol{B}(\boldsymbol{x}(0)) \cdot \boldsymbol{B}(\boldsymbol{x}(L)) \, \rangle \tag{2.2.1}$$

where L_c is the correlation length, $\boldsymbol{B}(\boldsymbol{x}(0))$ is the magnetic field at a random starting point, and $\boldsymbol{B}(\boldsymbol{x}(L))$ is the field at a point displaced a distance L along a fixed axis with respect to the starting point. Inserting the result of Eq. (2.1.1) into (2.2.1) yieding

$$L_c B_{\text{rms}}^2 = \pi \int_0^{\infty} \frac{\mathrm{d}k}{k} B^2(k), \tag{2.2.2}$$

then using the result from (2.1.8) and inserting $L = 2\pi/k$, the coherence length is found to be

$$L_c = \frac{1}{2} L_{\text{max}} \frac{\gamma - 1}{\gamma} \frac{1 - (L_{\text{min}}/L_{\text{max}})^{\gamma}}{1 - (L_{\text{min}}/L_{\text{max}})^{\gamma - 1}} \,. \tag{2.2.3}$$

For the Kolmogorov spectrum there are two interesting approximations to the coherence length. For a narrow-band spectrum, where $L_{\min} \sim L_{\max}$, the coherence length is approximated as $L_c \simeq L_{\max}/2$. When the band is broad, i.e. $L_{\min} \ll L_{\max}$, the coherence length is found to be approximately $L_c \simeq L_{\max}/5$.

Numerical approximation of the Turbulent Magnetic Field

When generating the turbulent magnetic field numerically, it is impossible to use an infinite number of Fourier modes. Giacalone and Jokipii (1994) presents an algorithm to approximate the theoretical turbulent magnetic field given in Eq. (2.1.1). It has later been discovered the algorithm presented in the 1994 paper had some mistakes regarding the rotation matrix, and the algorithm used here follows Tautz (2012) and Andersen (2017). Notable changes from Giacalone and Jokipii (1994) is that the initial wave-vector is changed to point along the z'-axis instead of the x'-axis. The equation for the algorithm then becomes

$$\boldsymbol{B}(\boldsymbol{r}) = \sum_{j=1}^{n_k} B(k_j)\boldsymbol{\zeta}_j e^{i(k_j z' + \beta_j)}, \tag{2.3.1}$$

where n_k is the number of Fourier modes, k_j is the wave number and β_j is a random phase of mode j. $B(k_j)$ is the amplitude of the mode and will follow the chosen Kolmogorov power spectrum, Eq. (2.1.7). The equation describes the superposition of the Fourier modes, each traveling in its own randomly chosen z'-direction. Each wave is a plane wave polarized in the plane given by the polarization vector

$$\boldsymbol{\zeta}_j = \cos(\alpha_j)\hat{\boldsymbol{e}}_{x'} \pm i\sin(\alpha_j)\hat{\boldsymbol{e}}_{y'}. \tag{2.3.2}$$

The primed unit vectors then form an orthonormal basis, coupled to the unprimed basis by

$$\begin{pmatrix} x' \\ y' \\ z' \end{pmatrix} = \begin{pmatrix} \cos\theta\cos\phi & \cos\theta\sin\phi & -\sin\theta \\ -\sin\phi & \cos\phi & 0 \\ \sin\theta\cos\phi & \sin\theta\sin\phi & \cos\theta \end{pmatrix} \begin{pmatrix} x \\ y \\ z \end{pmatrix}. \tag{2.3.3}$$

As each mode travels in a randomly chosen direction, θ and ϕ needs to be chosen randomly. The same goes for the polarization vector, where a random choice for the sign is also needed. Thus, for a single instance of the turbulent magnetic field, 5 random numbers are needed for each mode j. The constraints are:

$$\begin{aligned} 0 \leq\ & \theta(k) \leq \pi, \\ 0 \leq\ & \phi(k) \leq 2\pi, \\ 0 \leq\ & \alpha(k) \leq 2\pi, \\ 0 \leq\ & \beta(k) \leq 2\pi, \end{aligned}$$

as well as the sign ($s = \pm$) which needs to have a 50/50 probability of being either + or -. Discussion of the probability distribution is presented in section 2.5.

Furthermore, to assure the wavenumbers are weighted equally for all scale sizes, the modes k_j are distributed logarithmically between $k_{\min}$ and $k_{\max}$. This is equivalent of making the assumption that the eddy currents transfer their energy into smaller scale size eddies with a constant scale ratio. Such an assumption is common when modelling hydrodynamic turbulence (Ruelle, 2017).

Normalization of the Algorithm

To generate a magnetic field with the desired field strength B_{rms}, the amplitude of the modes $B(k)$ needs to be normalized over the Kolmogorov power spectrum given by Eq. (2.1.7). The normalization here follows the method of Giacalone and Jokipii (1994), using $B(k)$ directly instead of normalizing the field $\Omega(k)$. The same method is also used by Andersen (2017), where it is shown that

$$B_{\text{rms}}^2 = \sum_{j=1}^{n_k} B^2(k_j) \tag{2.4.1}$$

by taking the mean square value of Eq. (2.3.1) and using the fact that

$$\langle (\boldsymbol{\zeta}_j e^{i(k_j z' + \beta_j)}) \cdot (\boldsymbol{\zeta}_j e^{i(k_j z' + \beta_j)})^* \rangle = 1 \tag{2.4.2}$$

and demanding $\langle \boldsymbol{B}^2(\boldsymbol{r}) \rangle = B_{\text{rms}}^2$. As the scale size is constant after distributing the k_j-values evenly on a logarithmic scale, using the Kolmogorov spectrum from Eq. (2.1.7), the amplitude can be written

$$\frac{B^2(k)}{B^2(k_{\min})} = \left(\frac{k}{k_{\min}} \right)^{-\gamma}. \tag{2.4.3}$$

Inserting into Eq. (2.4.1) and solving for $B(k_{\min})$ gives

$$B(k_{\min}) = \frac{B_{\text{rms}}}{\sum_{j=1}^{n_k} \left(\frac{k}{k_{\min}} \right)^{-\gamma/2}} \tag{2.4.4}$$

which is the normalized value for $B(k_{\min})$. This normalization requires the field to be isotropic, which will be discussed in section 2.5.

The calculated turbulent magnetic field is complex, while it should be real. To get the real turbulent magnetic field, the real part of the calculated field is taken. However, this changes the RMS-value of the field. From the fact that $\langle \boldsymbol{x} \cdot \boldsymbol{x}^* \rangle = \langle \text{Re}^2(\boldsymbol{x}) \rangle + \langle \text{Im}^2(\boldsymbol{x}) \rangle$ and Eq. (2.1.5),

$$B_{\text{rms}}^2 = \langle \text{Re}^2(\boldsymbol{B}) \rangle + \langle \text{Im}^2(\boldsymbol{B}) \rangle \tag{2.4.5}$$

is found. Taking the mean square of $\boldsymbol{\zeta} e^{i(kz'+\beta)}$ it can be shown that $\langle \mathrm{Re}^2(\boldsymbol{B})\rangle = \langle \mathrm{Im}^2(\boldsymbol{B})\rangle$, which in turn gives

$$\langle \mathrm{Re}^2(\boldsymbol{B})\rangle = \tfrac{1}{2} B_{\mathrm{rms}}^2. \tag{2.4.6}$$

This leads to a change on the l.h.s. of Eq. (2.4.1) by a factor 1/2. Inserting this into Eq. (2.4.4) gives the final, normalized factor

$$B(k_{\mathrm{min}}) = B_{\mathrm{rms}} \left(\frac{2}{\sum_{j=1}^{n_k} \left(\frac{k_j}{k_{\mathrm{min}}} \right)^{-\gamma}} \right)^{1/2}. \tag{2.4.7}$$

Isotropy of the Turbulent Magnetic Field

Both Tautz (2012) and Andersen (2017) thoroughly discuss the isotropy of the magnetic field generated by the algorithm in section 2.3. A brief recapitulation of the discussion and conclusion is given here, to support the validity of the results derived by using the algorithm. The rest of the section follows the method in Andersen (2017).

First it is important to note that the proper isotropic field is given for a continuous integral over an infinite number of Fourier modes, meaning a numerical approximation will need as many discrete modes as is feasible, to achieve approximate isotropy. In the discussion of the isotropy it is assumed that n_k is large enough to make this assumption. Mathematically the expression for isotropy with zero mean, is that the magnetic field satisfies

$$\langle \boldsymbol{B}(\boldsymbol{r})\rangle = \boldsymbol{0} \tag{2.5.1}$$

and

$$\langle |B_x(\boldsymbol{r})\hat{\boldsymbol{e}}_x|^2\rangle = \langle |B_y(\boldsymbol{r})\hat{\boldsymbol{e}}_y|^2\rangle = \langle |B_z(\boldsymbol{r})\hat{\boldsymbol{e}}_z|^2\rangle = \frac{1}{3} B_{\mathrm{rms}}^2 \,. \tag{2.5.2}$$

For each mode k_j, $\boldsymbol{\zeta}_j$ is constant and complex and $B(k_j)$ is constant. For the total field to have zero mean

$$\langle \boldsymbol{\zeta}_j e^{i(k_j z'+\beta_j)}\rangle = 0 \tag{2.5.3}$$

is needed. This holds if the magnetic field spans a distance much larger than the largest magnetic eddies, i.e. $e^{i(k_j z'+\beta_j)}$ completes several cycles. Thus Eq. (2.5.1) is satisfied when $k_j|z'|_{max} \gg 2\pi$. From the fact that $\boldsymbol{B}$ is isotropic if all $\boldsymbol{k}$'s are isotropic, using $\hat{k} = \hat{z}'$ and $\boldsymbol{k} = k\hat{k}$, Eqs. (2.5.1) and (2.5.2) lead to

$$\langle \boldsymbol{k}\rangle = \langle \sin\theta\cos\phi\rangle \hat{\boldsymbol{e}}_x + \langle \sin\theta\sin\phi\rangle \hat{\boldsymbol{e}}_y + \langle \cos\theta\rangle \hat{\boldsymbol{e}}_z = \boldsymbol{0} \tag{2.5.4}$$

Table 2.1: Probability distribution and parameter intervals for the random variables in the algorithm for the turbulent magnetic field.

Parameter	Interval	Probability distribution
α	$0 < \alpha < 2\pi$	$p(\alpha) = 1/2\pi$
β	$0 < \beta < 2\pi$	$p(\beta) = 1/2\pi$
θ	$0 < \theta < \pi$	$p(\theta) = \sin(\theta)/2$
ϕ	$0 < \phi < 2\pi$	$p(\phi) = 1/2\pi$
$\pm$	$\{+, -\}$	$p(+) = 0.5$, $p(-) = 0.5$

and

$$\langle \sin^2\theta \cos^2\phi \rangle = \langle \sin^2\theta \sin^2\phi \rangle = \langle \cos^2\theta \rangle = \frac{1}{3}. \tag{2.5.5}$$

It is clear from Eq. (2.5.5) that $\langle \sin^2\theta \rangle = 2/3$. With the requirement that $0 < \theta(k) < \pi$ has a zero mean, the probability distribution has to be $p(\theta) = \sin(\theta)/2$. As $\langle \sin^2\theta \rangle = 2/3$, from Eq. (2.5.5) it is then given that $\langle \cos^2\phi \rangle = \langle \sin^2\phi \rangle = 1/2$, which makes the first two terms equal 1/3. This gives the probability distribution of $0 < \phi(k) < 2\pi$ as a uniform, flat distribution $p(\phi) = 1/2\pi$.

With these restrictions, $\boldsymbol{k}$ is isotropic for all Fourier-modes, and Eq. (2.1.4) holds. Now by inserting Eqs. (2.1.5) and (2.3.1) into (2.5.2), for each component

$$\langle |B_l(\boldsymbol{r})\hat{\boldsymbol{e}}_l|^2 \rangle = \sum_{j=1}^{n_k} B^2(k_j) \langle \left| \left[\boldsymbol{\zeta}_j e^{i(k_j z' + \beta_j)} \right]_l \right|^2 \rangle \tag{2.5.6}$$

with $\left[\boldsymbol{\zeta}_j e^{i(k_j z' + \beta_j)} \right]_l$ being the $\hat{\boldsymbol{e}}_l$ component of $\hat{\boldsymbol{B}}$. Eq. (2.5.6) shows that if the mean square value of the $\hat{\boldsymbol{e}}_l$ component equals 1/3, Eqs. (2.5.1) and (2.5.2) are satisfied and the field is isotropic.

The primed coordinate system is orthonormal, making $\boldsymbol{\zeta}$ and $e^{i(k_j z' + \beta_j)}$ independent. This gives

$$\langle \left| \left[\boldsymbol{\zeta}_j e^{i(k_j z' + \beta_j)} \right]_l \right|^2 \rangle = \langle \left| \left[\boldsymbol{\zeta}_j \right]_l \right|^2 \cdot \left| e^{i(k_j z' + \beta_j)} \right|^2 \rangle = \langle \left| \left[\boldsymbol{\zeta}_j \right]_l \right|^2 \rangle \tag{2.5.7}$$

where it is used that $\langle \left| e^{i(k_j z' + \beta_j)} \right|^2 \rangle = 1$ when $k_j z' \gg 2\pi$ as previously assumed. Setting Eq. (2.5.7) equal to 1/3, and using Eq. (2.3.2) together with the rotation matrix in Eq. (2.3.3),

$$\langle \zeta_x^2 \rangle = \langle \sin^2\alpha \cos^2\theta \cos^2\phi + \sin^2\alpha \sin^2\phi \rangle = \frac{1}{3}, \tag{2.5.8}$$

$$\langle \zeta_y^2 \rangle = \langle \sin^2\alpha \cos^2\theta \sin^2\phi + \sin^2\alpha \cos^2\phi \rangle = \frac{1}{3}, \tag{2.5.9}$$

$$\langle \zeta_z^2 \rangle = \langle \sin^2\alpha \sin^2\theta \rangle = \frac{1}{3}, \tag{2.5.10}$$

where $\zeta_l^2 = |\boldsymbol{\zeta}_l|^2$. From Eqs. (2.5.4) and (2.5.5) together with the constraint $0 < \alpha < 2\pi$, it is found that $\langle \sin^2 \alpha \rangle = \langle \cos^2 \alpha \rangle = 1/2$. This gives a flat probability distribution $p(\alpha) = 1/2\pi$. The sign in $\boldsymbol{\zeta}$ decides if the polarization is left- or right-circular. To avoid left- or right-chirality in the field, the sign then has to have a 50:50 probability distribution. β is a phase shift of the Fourier mode with respect to the origin and in order for the field to be random β has to be uniformly distributed between 0 and 2π.

Table 2.1 summarizes the probability distributions that make the field isotropic. This isotropy is found in Andersen (2017), while Tautz (2012) argues the field generated is not isotropic, and concludes $\langle \zeta_l^2 \rangle$ equals 3/8 for x and y, and 1/4 for z. This can be achieved by choosing $p(\theta) = 1/2\pi$. Thus, the argument made by Tautz (2012) holds, but it is also possible to generate an isotropic turbulent magnetic field using the same algorithm, by choosing the proper probability distributions as shown.

Particle Movement in a Magnetic Field

A charged particle moving in a magnetic field is influenced by the force

$$\boldsymbol{F}_M = q\boldsymbol{v} \times \boldsymbol{B}, \tag{2.6.1}$$

assuming there's no electric field ($\boldsymbol{E} = \boldsymbol{0}$) and with q being the charge of the particle. Using Newton's second law the equation of motion of a charged particle is given as

$$\boldsymbol{F}_M = \frac{d\boldsymbol{p}}{dt} = q\boldsymbol{v} \times \boldsymbol{B}. \tag{2.6.2}$$

For high energy particles the relativistic momentum is given by

$$\boldsymbol{p} = \gamma_l m \boldsymbol{v} \tag{2.6.3}$$

where γ_l is the Lorentz factor. As the change in momentum is proportional to the cross product of the velocity and the magnetic field, the acceleration of the particle will be perpendicular to magnetic field line.

Magnetic Field Gradient

For a charged particle moving in a magnetic field that has a gradient, the adiabatic invariant is the integral

$$I = \frac{1}{2\pi} \oint \mathbf{P}_t \cdot d\mathbf{r}, \tag{2.7.1}$$

integrated over a complete period of the motion perpendicular to $\hat{b}$, where $\hat{b}$ is the magnetic field unit vector (Landau and Lifshitz, 1971, §21). Here $\mathbf{P}_t$ is projection of the generalized momentum onto the plane that is perpendicular to $\hat{b}$. Calculating this integral, following section 21 in Landau and Lifshitz (1971), the adiabatic invariant can be shown to be

$$I = \frac{3cp_t^2}{2qB}, \tag{2.7.2}$$

giving $\Delta p_t \propto \Delta\sqrt{B}$, where p_t is the momentum perpendicular to $\hat{b}$. If the mass is constant, this is equivalent of $\Delta v_\perp \propto \Delta\sqrt{B}$. Furthermore, as the velocity has to be constant and $v^2 = v_\parallel^2 + v_\perp^2$, the parallel velocity changes proportional to the perpendicular velocity. Due to this, any particle moving in the direction of increased field strength will be decelerated in the parallel directions. When $v_\parallel$ becomes zero, the particle is reflected, and begins moving in the direction of smaller field strength. This effect does not depent on the sign of the particles charge.

Magnetic Field Curl

A particle propagating in a curled magnetic field will experience a drift velocity. Following Landau and Lifshitz (1971) section §22, the effect of the curl is derived by assuming the particle is originally moving in a circular orbit. This trajectory can be written as $\mathbf{r} = \mathbf{R}(t) + \zeta(t)$ where $\mathbf{R}(t)$ is the position vector of the guiding center and $\zeta(t)$ describes the rotational motion about the guiding center. $\mathbf{R}$ can be considered to change slowly, while ζ is rapidly changing. Averaging the force, Eq. (4.2.4), over one period of the motion about the guiding center, and expanding $\mathbf{B}(r)$ in powers of q as $\mathbf{B}(\mathbf{r}) = \mathbf{B}(\mathbf{R}) + (\zeta \cdot \nabla)\mathbf{B}(\mathbf{R})$, the averaging of the force removes the first order terms. The second order terms contribute a force

$$\mathbf{F_{curl}} = q\dot{\zeta} \times (\zeta \cdot \nabla)\mathbf{B}. \tag{2.8.1}$$

Applying that for a circular orbit $\zeta = \Omega\zeta \times \hat{b}$ and $|\zeta| = v_\perp/\Omega$, the force becomes

$$\mathbf{F}_{\text{curl}} = -\frac{mv_\perp^2}{2B}\left(\hat{b} \times \nabla\right) \times \mathbf{B}. \tag{2.8.2}$$

Using that $\nabla \cdot \mathbf{B}(\mathbf{R}) = \nabla \times \mathbf{B}(\mathbf{R}) = 0$, the force can be written as

$$\mathbf{F_{curl}} = \frac{mv_\perp^2}{2\rho}\hat{n}, \tag{2.8.3}$$

where ρ is the curvature of the magnetic field line at the given point, and $\hat{n}$ is the unit vector pointing from the center of this curvature towards the point at

which the curvature is calculated. Now, if the particle also has a parallel velocity, $\mathbf{F}_{\text{curl}}$ can be further simplified by changing to the instantaneous reference frame rotating about the center of curvature. Using this frame of reference, with an angular velocity $v_\parallel/\rho$, the particle has no parallel velocity. However, there is now a centrifugal force $qmv_\parallel^2/\zeta$. The perpendicular force is then

$$\mathbf{F}_\perp = \frac{m}{\rho}\left(v_\parallel^2 + \frac{v_\perp^2}{2}\right)\hat{n}, \tag{2.8.4}$$

which is equivalent of a constant electric field of strength $\mathbf{F}_\perp/q$. From this the drift velocity

$$\mathbf{v}_d = \frac{1}{\rho\Omega}\left(v_\parallel^2 + \frac{v_\perp^2}{2}\right)\hat{n}\times\hat{b} \tag{2.8.5}$$

is found. The sign of the drift velocity depends on the sign of the charge of the propagated particle.

Larmor-radius

From Eq. (2.6.2) it can be seen that a particle moving in a uniform magnetic field will portray a helical trajectory. The component of the velocity parallel to the magnetic field, $v_\parallel$, will not be affected by the magnetic force, whilst the perpendicular component, $v_\perp$, will change according to the force. Using the fact that $a = v_\perp^2/r$ for circular motion the radius of the trajectory can be calculated as

$$R_g = \frac{\gamma_l m v_\perp}{|q|B}. \tag{2.9.1}$$

The radius R_g is known by a few names, most commonly the gyro-radius or the Larmor-radius. The absolute value of the charge is taken as the radius can't be negative. For high energy particles the relativistic energy is given by $E = \gamma_l mc^2$ where c is the speed of light in vacuum. A more practical way of writing the Larmor-radius is

$$R_g = \frac{\beta_\perp}{cq}\frac{E}{B} \tag{2.9.2}$$

where $\beta_\perp = v_\perp/c$. For a purely turbulent magnetic field the local Larmor-radius can be calculated using $B = B_{\text{rms}}$, while in a magnetic field consisting of a coherent and turbulent part in superposition, $B = B_0 + B_{\text{rms}}$ where B_0 is the strength of the coherent field. If $R_g \ll L_c$ (the correlation length) the particle will experience the field as approximately constant, leading to a helical motion about the magnetic field lines. In the opposite case, $R_g \gg L_c$, the magnetic field would change too rapidly for the particle to be heavily influenced. For a zero mean field this would

lead to small deflections over scale lengths $\sim L_c$, giving a trajectory consisting of straight lines with small deflections.

Diffusion Tensor and Coefficients

CRs diffuse in the Galactic magnetic field depending on the energy of the ray and the strength of the magnetic field. Outside of shock regions (acceleration zones) such diffusion is commonly described by a diffusion coefficient $D(E) = D_0(E/E_0)^\beta$. The coefficient is usually estimated for two regimes, one small-angle scattering regime where $D(E) \propto E^2$, and one large-angle scattering regime where $D(E) \propto E^{2-\gamma}$. Here γ is still the energy-spectrum coefficient, which is 5/3 for the Kolmogorov spectrum, and β is equal to 2 and 1/3 for the two energy regimes respectively. This and the rest of this section is cited from Giacinti et al. (2018) unless otherwise specified.

Diffusion is measured in area covered per time unit, leading to a diffusion tensor on the form

$$D_{ij} = \lim_{t\to\infty} \frac{\langle x^{(i)} x^{(j)} \rangle}{2t}, \tag{2.10.1}$$

as given in Subedi et al. (2017), equation (8). For a purely isotropic field the eigenvalues, also known as the diffusion coefficients, d_x, d_y and d_z describes diffusion in the respective directions. The eigenvalues are found by diagonalizing D_{ij} and taking the trace of the diagonalized tensor. To calculate the diffusion tensor from a given set of trajectories, it is not enough to look at a single trajectory. Instead, the average over a significant amount of particles has to be calculated. For the magnetic field to be isotropic, the time spanned needs to be large enough so that all particles travel multiple times the coherence length L_c. Using t_* to denote a time fulfilling this requirement,

$$D_{ij} = \frac{1}{2Nt_*} \sum_{a=1}^{N} x_i^{(a)} x_j^{(a)} \tag{2.10.2}$$

gives the averaged diffusion tensor, with N being the number of particles and $x_i^{(a)}$ being the x_i-component of particle a. The average diffusion coefficient is then given as

$$D = \frac{1}{6Nt_*} \sum_{a=1}^{N} \boldsymbol{x}^{(a)} \cdot \boldsymbol{x}^{(a)}. \tag{2.10.3}$$

As one instance of a turbulent magnetic field could give extremal values for the diffusion tensor, the calculated values should be averaged over several instances of the turbulent magnetic field as $D = \frac{1}{M} \sum_M D^{(b)}$ where M is the number of instances used and $D^{(b)}$ is the average diffusion coefficient calculated by Eq. (2.10.3)

for instance b of the turbulent magnetic field (Giacinti et al., 2012). It is also possible to derive the functional dependence of the diffusion coefficient for an isotropic magnetic field. This functional is given as

$$D = \frac{cL_0}{3}\left[\left(\frac{R_g}{L_0}\right)^{2-\gamma} + \left(\frac{R_g}{L_0}\right)^2\right], \tag{2.10.4}$$

where $R_g(E) = L_0$ is the condition determining the transition from $D(E) \propto E^2$ to $D(E) \propto E^{2-\alpha}$ ($\beta = 2 \to 1/3$). The length L_0 in general needs to be numerically determined, but is expected to be $L_0 \propto L_c$, where L_c is the coherence length. A good fit has been found to be $L_0 \simeq L_c/(2\pi)$.

Transition Time

The transition time describes when the diffusion reaches the isotropic limit, i.e. when the particles transition from the anisotropic regime to the isotropic regime. It can be approximated as

$$\tau \sim \frac{4D}{c^2}. \tag{2.11.1}$$

CHAPTER 3

IMPLEMENTATION OF COSMIC RAY DIFFUSION SIMULATION

In this chapter the various methods used to simulate the diffusion of CRs are described, and the results of the simulations are presented. The code written for this project was developed by the author of the report, using the Random Number Generator (RNG) and different integrators from Press et al. (2007). C++ was used in this project, and the code can be found at Github.com/odde92/master_thesis.

Implementation

3.1.1 Generating the Turbulent Magnetic Field

Generating the magnetic field follows the numerical method described in section 2.3. Eq. (2.3.1) is implemented through several steps. The first step is to generate the random numbers for the parameters in table 2.1, for the chosen amount of modes. These phases are only chosen at the start of the program, and are constant for each instance of the magnetic field. To generate the random numbers an RNG from (Press et al., 2007, p. 342-343) was used. When a new instance of the magnetic field is generated, all phases have to be randomly chosen anew. After the phases have been initialized, the normalization of $B(k)$ can be carried out, as described in section 2.4. The sum in Eq. (2.4.7) is calculated first, before $B(k_{\min})$ is determined. When $B(k_{\min})$ has been found, the amplitude of each mode $B(k_j)$ can be calculated with Eq. (2.4.3).

After the normalization is performed, and the amplitude of the modes has been found, Eq. (2.3.1) can be calculated. As the equation describes a vector, each component B_x, B_y and B_z in the non-rotated system is calculated separately. As

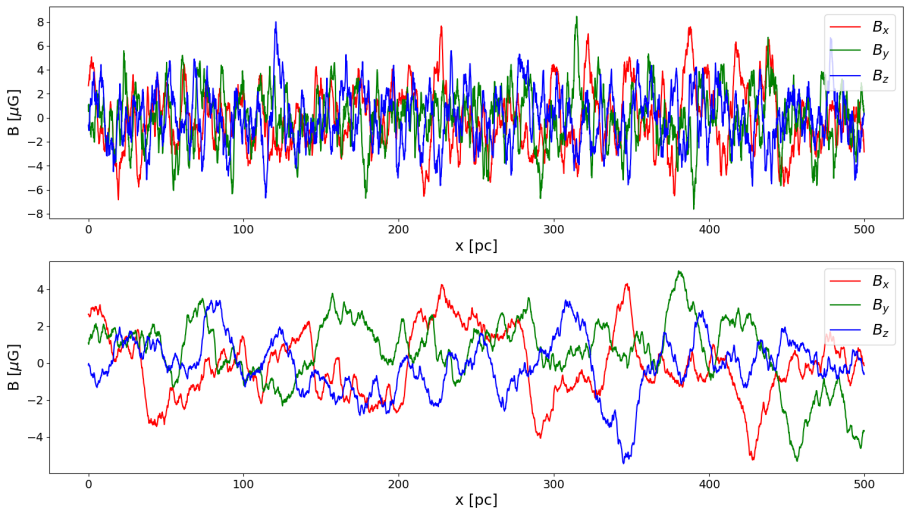

Figure 3.1: The x-, y- and z-components of two magnetic fields, generated with the same set of random phases, over a length of 500 pc in the x-direction. The top figure has $L_{\max} = 10$ pc while the lower figure has $L_{\max} = 150$ pc The difference in coherence length is easily visible.

the field is complex, it is needed to keep track of both the real and imaginary values. The exponent and amplitudes are not vectors and can be multiplied together as complex scalars. $\boldsymbol{\zeta}$ is the only vector in the equation, and is defined for the x', y'-plane. Projecting this onto the x, y and z-axis by using the rotation matrix in Eq. (2.3.3), the polarization in the non-rotated system is found. At last, the total magnetic field in each direction is found by summing up the product of the complex scalars and $\zeta_{(x/y/z)}$ for all modes. Since the actual turbulent magnetic field is real, and the field calculated to this point is complex, the final step is to take the real part of the calculated field. Taking the real part of the field is accounted for in Eq. (2.4.7), and why this can be done is explained in section 2.4. Figure 3.1 shows two example magnetic fields that were generated using the same random phases, but different coherence lengths, plotted for a straight trajectory of 500 pc in the x-direction.

3.1.2 Cosmic Ray Initialization

The initial condition of each simulated CR was set in two steps. The mass, charge and energy of each particle was set before compilation of the program. The initial

position was always chosen, in this chapter, as the center of the coordinate system, i.e. $\mathbf{x}_0 = \{0, 0, 0\}$. This left only the CRs' velocity to be decided. The velocities had to be chosen in a random direction, uniformly distributed on a sphere in three-dimensional Euclidean space. As such the same probability distribution was used for the velocity, as was used for the random modes in section 2.5, listed in table 2.1. Implementing this, the velocities where chosen as

$$\begin{aligned} v_x &= v\cos(\Phi)\sin(\Theta), \\ v_y &= v\sin(\Phi)\sin(\Theta), \\ v_z &= v\cos(\Theta), \end{aligned}$$

where the angles are randomly chosen and the speed v was calculated using $v = c\sqrt{1 - 1/\gamma_l^2}$. The Lorentz-factor was decided by the mass and energy of the particle, and was found using $\gamma_l = E/mc^2$, where both the mass and energy were chosen at compile-time.

3.1.3 Calculating Cosmic Ray Trajectories

To calculate the CR trajectories a numerical integrator from Press et al. (2007) was implemented. Equation (4.2.4) was used as the Ordinary Differential Equation (ODE), on the form

$$\frac{d^2\mathbf{x}}{dt^2} = \frac{q}{\gamma_l m}\mathbf{v} \times \mathbf{B} \tag{3.1.1}$$

which calculates $d\mathbf{x}/dt$ step by step. Here $\mathbf{x}$ is the position vector of the particle. As it is a vector equation, (3.1.1) gives three actual equations, each dependent on the two others due to the cross term. The numerical methods tested were all Runge-Kutta (RK)-methods, and the presented results were simulated using a Bulirsch-Stoer RK-method.

Finding the position of the CRs through the trajectory was done using that

$$\frac{d\mathbf{x}}{dt} = \mathbf{v} \tag{3.1.2}$$

where $\mathbf{v}$ is the velocity caculated in Eq. (3.1.1).

3.1.4 Determining the Diffusion Tensor and Coefficients

The diffusion coefficient is calculated by Eq. (2.10.2). Since the matrix is symmetric, it is enough to find the upper half, including the diagonal, of the matrix. The sum in Eq. (2.10.2) was calculated by adding the value for each particle simulated together in a vector. This was done at each desired point in time (in this report:

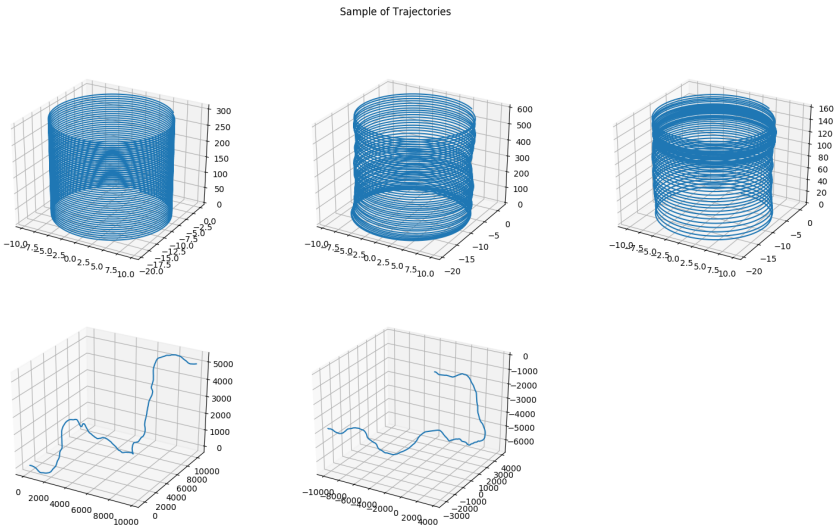

Figure 3.2: A few sample trajectories generated by the RK4-method. All fields are simulated using a proton with $E = 1 \cdot 10^{16}$eV, with all axes being in parsec. The same instance of the magnetic field has been used. The first three plots have a regular component of 1 µG. The second and third plots also have a turbulent field with $B_{\text{rms}} = 0.1\mu$G and $L_{\text{max}} = 10\,\text{pc}$ and 150 pc respectively. The last two trajectories have $B_{\text{rms}} = 1\mu$G without a regular field and $L_{\text{max}} = 10\,\text{pc}$ and 150 pc respectively.

1, 2, 3, ... , 10, 20, 30, ... , 100, 200, 300, ... , 10^n years), for each instance of the magnetic field. MPI was used to run one instance of the magnetic field on one thread, for a total of 10 threads calculating and one thread used to add the results from each instance together.

After completing the sum over the chosen amount of particles, the sum was divided according to Eq. (2.10.2) and sent to the main thread. When all diffusion tensors of the different magnetic field instances had been calculated, the diffusion coefficients, or eigenvalues $d_x^{(b)}$, $d_y^{(b)}$, $d_z^{(b)}$, of all tensors were calculated, as well as the average diffusion coefficient $D^{(b)}$ from Eq. (2.10.3). To find the average diffusion coefficients over all instances, all diffusion coefficients were averaged as

$$d_i = \frac{1}{M} \sum_{b=1}^{M} d_i^{(b)}. \tag{3.1.3}$$

This was done for each point in time where the coefficients had been recorded. The same method was used to find the average over all instances of the average diffusion coefficient D.

Table 3.1: List of parameters used in the simulations of proton diffusion in the Galactic TMF.

Parameter	Value	Unit	Description
m	938.2720813	MeV/c^2	Proton mass
q	1	$1.602 \cdot 10^{-19}$C	Charge in # of elementary charges
B_{rms}	4.0	µG	TMF RMS strength
M	10	#	Number of MF instances
n_k	100	#	Number of modes
N_1	1000	#	Number of particles 1
N_2	100	#	Number of particles 2
$L_{\text{max, 1}}$	150	pc	Max scale size 1
$L_{\text{max, 2}}$	10	pc	Max scale size 2
L_{min}	0.027	pc	Min scale size
rtol_1	$1 \cdot 10^{-5}$	m/s	Relative error tolerance 1
$\text{atol}_{1/2}$	$\text{rtol}_{1/2}$	m/s	Absolute error tolerance

With all diffusion coefficients d_x, d_y and d_z, as well as all average diffusion coefficients D calculated, the values were plotted and the results could be compared to previous results of the diffusion coefficients.

Results and Discussion

In this section the results of the simulations are presented. They are discussed in relation to the theory presented in chapter 2 as well as results presented in Giacinti et al. (2012) and Giacinti et al. (2018). In table 3.1 the different parameters used in the simulations are listed.

One of the main objectives of this project was to simulate the diffusion of protons in a turbulent magnetic field. How the diffusion behaves compared to the theory and previous results is discussed in section 3.2.1 and 3.2.2. Furthermore, the transition time and amplitude of the results are discussed in sections 3.2.3 and 3.2.4.

3.2.1 Behavior of the Diffusion Coefficients

Diffusion of protons in a turbulent magnetic field has been described in section 2.10. Combining this with the isotropic characteristics of the numerical algorithm used to generate the turbulent magnetic field, it is expected that the diffusion is isotropic only when the protons have travelled a distance $|\boldsymbol{r}| \gg L_{\text{c}}$. If this is

the case the diffusion is expected to be approximately equal in all directions, as the protons experience the turbulent magnetic field as isotropic and homogeneous under this condition. The diffusion being approximately equal in all directions means the diffusion coefficients d_x, d_y and d_z are approximately equal.

As long as $|\boldsymbol{r}| \lesssim$ a few L_c the protons experience the field as approximately constant. For a randomly generated turbulence, this suggests that a proton starting from the origin interacts with a magnetic field in a certain direction. The diffusion under this condition is then expected to be biased in a random direction. In terms of the diffusion coefficients, they are expected to diverge in this period.

In the middle of the two previous assumptions, i.e. where $|\boldsymbol{r}| \sim$ a few L_c, the divergence is expected to stop, and the diffusion coefficents should start converging. However, they should not reach convergence before having travelled several L_c.

Figure 3.3 shows the calculated diffusion tensor for 1000 protons simulated for $1 \cdot 10^5$ years, averaged over 10 instances of the turbulent magnetic field. The overall impression is that the diffusion behaves as expected. In the beginning of the simulation the protons propagate in the turbulent magnetic field under the condition $|\boldsymbol{r}| \lesssim$ a few L_c. The theoretical expectation is met as the diffusion coefficients diverge. It does, however, take some time before d_1 and d_2 diverge from each other, and they follow the same trajectory until $t \simeq 10$ years. They continue diverging until $t \simeq 4 \cdot 10^2$ years. After this all three coefficients are increasing, with d_1 and d_2 increasing rapidly compared to d_3. Still, d_3 increases steadily through this entire period. When $t \simeq 1 \cdot 10^3$ years, d_3 starts decreasing. At this point d_2 has mostly flattened out, while d_1 is still increasing. In total this is the point where the diffusion coefficients begin converging. This indicates that $|\boldsymbol{r}| > \sim$a few L_c. From this point forward the coefficients continue converging until $t \simeq 9 \cdot 10^4$ years, where they flatten out. There is still a difference between the three coefficients after they have stopped converging, with the average diffusion coefficient $D = 1.19 \cdot 10^{29}\,\mathrm{cm}^2/\mathrm{s}$. The largest difference is between d_1 and d_3, and is a factor $d_3/d_1 \sim 10$. As the diffusion coefficients are of the scale $\sim 1 \cdot 10^{28}\,\mathrm{cm}^2/\mathrm{s}$, a factor difference of 10 is significant. Another way to look at it, is to say that the protons diffuse 10 times more in the d_z-direction than in the d_x-direction. This difference suggests the field is anisotropic even after $1 \cdot 10^5$ years, with the particles travelling a distance $|\boldsymbol{r}| \gg L_\mathrm{c}$. From the theory in section 2.10 this anisotropy is not expected.

Comparing the result in figure 3.3 to figure 1 in Giacinti et al. (2012) (see figure C.1 in Appendix C), where the same values for B_rms, L_max, γ and E are used, the behavior of the coefficients are similar. The graph in Giacinti et al. (2012) starts at $t = 1 \cdot 10^2$ years and ends at $t = 1 \cdot 10^5$ years, and thus doesn't show how the coefficients behave in the earliest stages of the simulation. Within the period shown in both graphs the behavior of the diffusion coefficients is practically identical,

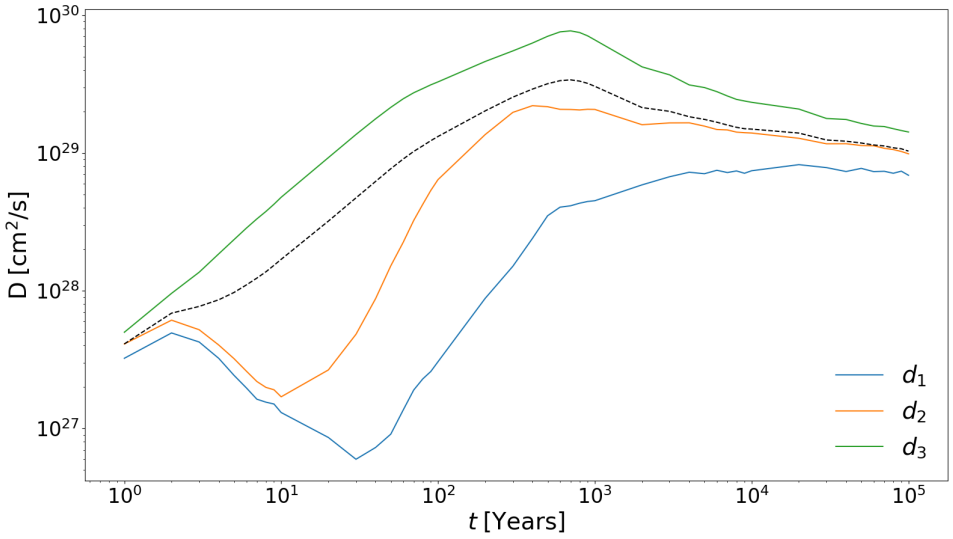

Figure 3.3: Eigenvalues of the diffusion tensor of a proton with $E = 1\,\text{PeV}$ and $L_{\text{max}} = 15\,\text{pc}$. d_1, d_2 and d_3 are the diffusion coefficients in the x-, $y-$ and z-directions respectively. The dotted line is the average diffusion coefficient calculated with Eq. (2.10.3). The same layout is used for all diffusion tensor plots.

showing strong anisotropy in the earliest years, and converging to more isotropic behavior towards the end. The same flattening of the coefficients happen close to $t = 1 \cdot 10^5$ years in both graphs, with neither graph reaching proper isotropic condition of $d_1 = d_2 = d_3$. In Giacinti et al. (2018) the factor $d_3/d_1 \sim 3.5$. While this factor is smaller than the factor $d_3/d_1 \sim 10$ derived from figure 3.3, it still shows a significant difference from the isotropic condition.

To further examine the behavior of the diffusion coefficients, simulations for higher energies were conducted. The results for $L_{\text{max}} = 150\,\text{pc}$ are shown in figure 3.4. The anisotropic behavior in the early times apparently drops off drastically from $E = 10\,\text{PeV}$ to $E = 100\,\text{PeV}$. Using Eq. (2.6.2) looking at $\frac{d\boldsymbol{v}}{dt} \propto \gamma_l^{-1}$, assuming the total velocity and B_{rms} are constant, the change in momentum is expected to decrease with a higher γ_l. Since higher energy is equivalent with a higher γ_l, it is then expected that $\frac{d\boldsymbol{v}}{dt}$ becomes smaller. As the particles simulated all start with a velocity in a random direction it is to be expected that anisotropic behavior is less apparent at higher energies. Giacinti et al. (2012) figure 3 (see figure C.3 in Appendix C)includes $E = 10\,\text{PeV}$ as the highest energy. Comparing this to the second panel in figure 3.4 the anisotropy is found to be smaller in Giacinti et al. (2012) than what is found here. Deriving the factors d_3/d_1 and

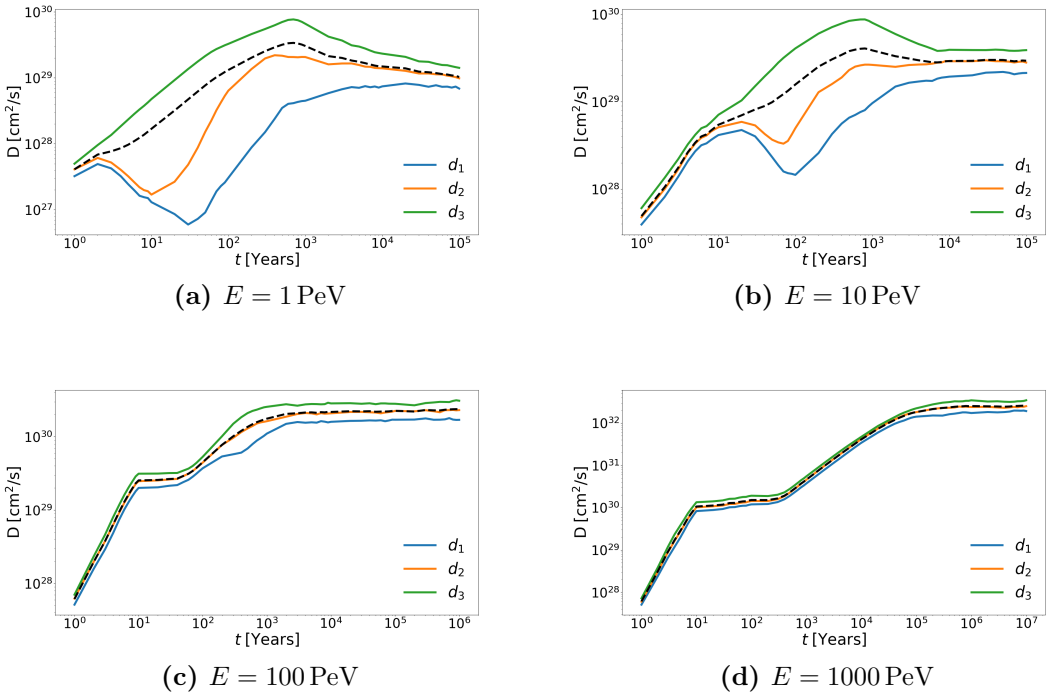

(a) $E = 1\,\mathrm{PeV}$ **(b)** $E = 10\,\mathrm{PeV}$

(c) $E = 100\,\mathrm{PeV}$ **(d)** $E = 1000\,\mathrm{PeV}$

Figure 3.4: Comparison of the diffusion tensor for different energies when $L_{\max} = 150\mathrm{pc}$. The energies range from $E = 1\,\mathrm{PeV}$ in the upper left panel to $E = 1000\,\mathrm{PeV}$ in the lower right panel.

comparing them, approximately the same relation is found as was found for $E = 1\,\mathrm{PeV}$.

While the anisotropic behavior of the diffusion coefficients compares excellently to Giacinti et al. (2012), both finding d_3/d_1 ∼a few hundred, there is still a disagreement with the theory regarding the isotropic limit. As stated in section 2.5 proper isotropy is only achieved using an infinite amount of Fourier modes. As the numerical approximation has to use a discrete, finite set of modes, this will induce an error compared to the theory. The more modes are used, the less error should be induced in the approximation. Andersen (2017) finds that using $n_k = 500$ modes should give a high degree of isotropy, while $n_k = 100$ should provide a sufficient degree of isotropy. A second, likely error source is the RK-solver. Each step is calculated using a step-size control that measures the local truncation error, demanding it to be within the limits *rtol* and *atol*. As the local truncation error is calculated using the total velocity change, there could be errors in the components of the velocities that are not identified. On the other hand, it could be argued that the errors should cancel when calculating the total velocity from the components. A counterargument to this again, is that the errors could cancel each other if for

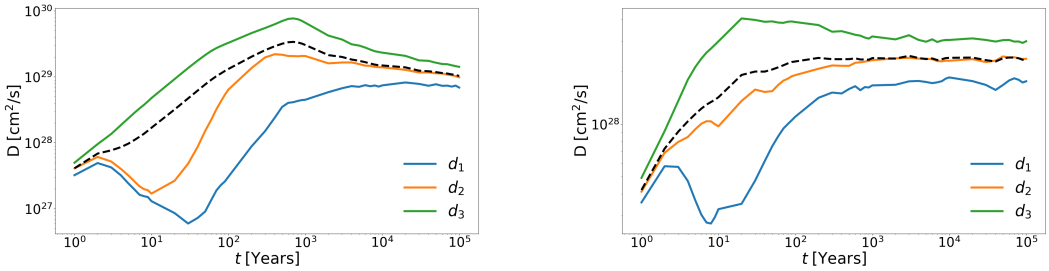

(a) $E = 1\,\mathrm{PeV}$, $L_{\max} = 150\,\mathrm{pc}$ **(b)** $E = 1\,\mathrm{PeV}$, $L_{\max} = 10\,\mathrm{pc}$

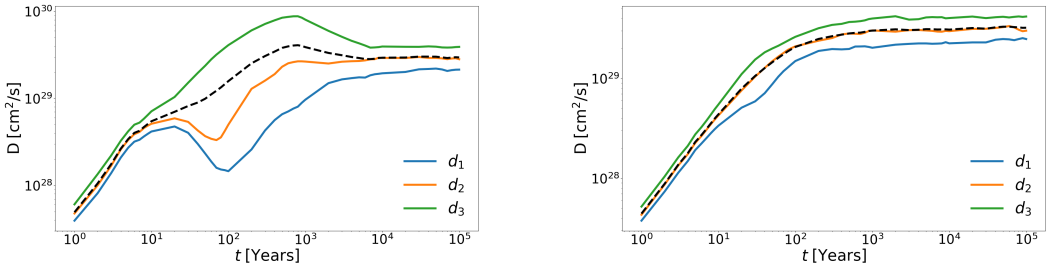

(c) $E = 10\,\mathrm{PeV}$, $L_{\max} = 150\,\mathrm{pc}$ **(d)** $E = 10\,\mathrm{PeV}$, $L_{\max} = 10\,\mathrm{pc}$

Figure 3.5: Comparison of the diffusion tensor when $L_{\max}$ is changed from 150 to 10 pc for $E = 1\,\mathrm{PeV}$ and $E = 10\,\mathrm{PeV}$. The lower energy is plotted in the two upper figures, while the higher energy is plotted in the two lower figures. Legend is the same as in figure 3.3.

example v_x is less than it should be and v_y is larger than it should, assuming v_z to be correct.

The approximation of an isotropic turbulent magnetic field using Eq. (2.3.1) and possible numerical errors in the implementation of the RK-solver then seem like the major contributors to the anisotropy shown in the graphs of figure 3.4 at $t = 1 \cdot 10^5$ years. Another source that is not to be written off is a simple programming error in the code. This could be anything from a constant being multiplied incorrectly to some undiscovered systematic mistake. One major error was found in the code towards the end of the project, along with several minor mistakes. This suggests there could be more mistakes in the program, but the behavior of the diffusion tensor suggests they would likely be minor. One last source of error to be mentioned is the possibility of numerical errors. As the program handles numbers spanning from $\sim 1 \cdot 10^{-17}\,\mathrm{m}$ to $\sim 1 \cdot 10^{30}\,\mathrm{cm}^2/\mathrm{s}$, there could be overflow when converting from one unit to the other, or when multiplying different factors together. Such overflows are expected to be handled by imposing a constraint on the local truncation error, but it should still be considered as a

possible source of error.

To further investigate the behavior of the diffusion coefficients, the simulations were run with different values for $L_{\max}$ and $L_{\min}$. For the two values considered for $L_{\max}$, two cases were tested for $L_{\min}$. The first value tested was $L_{\min} = 0.027\,\mathrm{pc}$, or $R_g(E = 1\,\mathrm{PeV})/10$. The second value was $R_g(E = 1\,\mathrm{PeV})/10^5$. Changing $L_{\min}$ was found to have no major effect on the diffusion tensor, and the final simulations were done using a constant $L_{\min} = R_g(E = 1\,\mathrm{PeV})/10$. This find is not surprising, as the small scale size Fourier modes only contribute minor perturbations to the turbulent magnetic field compared to the larger scale size modes. On the other hand it was important to test the scenario for $L_{\max} = 10\,\mathrm{pc}$, as claiming this fulfills the condition $L_{\max} \gg L_{\min}$ would be dubious without testing.

In figure 3.5 the diffusion coefficients for $E = 1\,\mathrm{PeV}$ and $E = 10\,\mathrm{PeV}$ are compared when $L_{\max}$ is varied. For the lower energy the anisotropy is prominent for both values of $L_{\max}$. However, the transition seems to happen earlier for $L_{\max} = 10\,\mathrm{pc}$. The transition time will be further discussed in section 3.2.3. There also seems to be a declining trend for the diffusion coefficients in this case, instead of convergence. When the energy is increased, the prominence of the anisotropic behavior rapidly declines for the lowest value of $L_{\max}$. However, it is still visible and happens at the same time as for the lower energy. As previously discussed, the magnitude of the anisotropy decreasing with higher energy is to be expected. When the scale size is reduced, so is the coherence length. When the energy is then increased, the number of coherence lengths travelled over a given period is proportionally increased. This suggests that the anisotropic behavior should indeed decrease more rapidly for smaller $L_{\max}$.

3.2.2 Filamentary Structure in the Intensity Plots

To visualize what the diffusion would look like, intensity plots were made by projecting the protons onto the xy-plane. These plots could then present how the diffusion evolved for the given energies and coherence lengths.

Figure 3.6 shows the intensity plot from the same simulation used to produce the graph in figure 3.3. The position of the protons are presented at $t = 1000\,\mathrm{years}$, $t = 2000\,\mathrm{years}$ and $t = 7000\,\mathrm{years}$. The filamentary structure is clearly shown in the first two panels, while the third panel shows how the protons have transitioned to an isotropic-like diffusion. The filamentary structures are expected while the protons are in the anisotropic regime, as they are forced in a certain direction until the effects of the turbulent magnetic field averages out. This is also in agreement with Giacinti et al. (2012), who finds the same filamentary structures in the anisotropic regime. Comparing the time where the proton positions were recorded to the diffusion coefficients in figure 3.3, the two first panels are found to be within the anisotropic regime, while the third panel is in the approximately

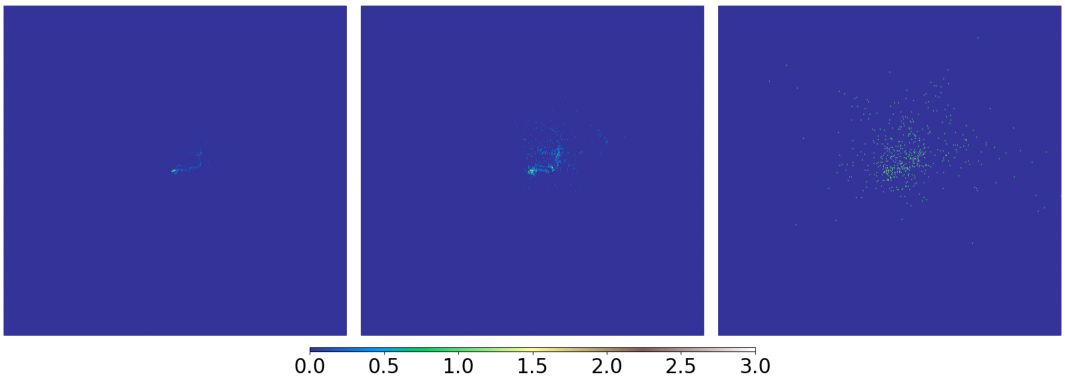

Figure 3.6: Intensity plot of 1000 protons' position projected onto the xy-plane. A brighter color means more particles are projected onto that area. In this plot $E = 1\,\text{PeV}$ and $L_{\text{max}} = 150\,\text{pc}$. The positions are recorded, from left to right, at times $t = 1000\,\text{years}$, $t = 2000\,\text{years}$ and $t = 7000\,\text{years}$, to show how the diffusion develops over time. The x and y axes are in parsec, and are scaled with respect to the furthest propagated particles in each direction.

isotropic regime.

To evaluate the findings from figure 3.4, the intensity plots for the same simulations were generated and are presented in figure 3.7. For the two lower energies the filamentary structures are clearly visible. When the energy is increased this behavior is less prominent. Comparing this to what was found for the diffusion coefficients, both results are in agreement with the theory and expectancy. The same behavior with respect to energy is found in Giacinti et al. (2012) figure 2 (see Figure C.2 in Appendix C), where intensity plots of protons with $E = 0.1 - 10\,\text{PeV}$ projected onto the xy-plane after $t = 500\,\text{years}$, $t = 2000\,\text{years}$ and $t = 7000\,\text{years}$. Comparing the behavior of the intensity plots, the filamentary structure is found in both cases.

For the different energy levels in figure 3.7, the protons are found to have travelled longer for higher energies. This is to be expected, as higher energy is equivalent of higher momentum. One thing to note is that for all three energies the particles seem to travel proportionally the same distance in the first two panels, with respect to the third. As the time difference between the panels is constant, this suggests the diffusion scales like $D(E) \propto E^{\beta}$ as suggested in section 2.10, with $\beta = 1/3$ or 2, depending on the diffusion regime.

Considering the results from figure 3.5, comparing the diffusion when changing L_{max} from $150\,\text{pc}$ to $10\,\text{pc}$, the anisotropic behavior is expected to be less prominent. This comparison is shown in figure A.2, comparing the diffusion when $E = 1\,\text{PeV}$ and $E = 10\,\text{PeV}$. For $L_{\text{max}} = 10\,\text{pc}$ it is hard to recognize any

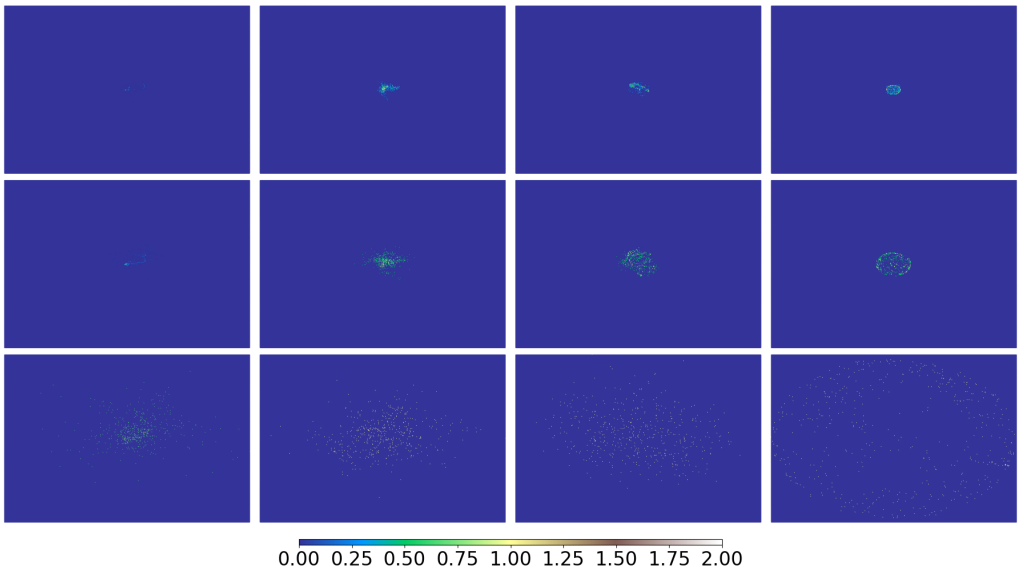

Figure 3.7: Comparison of the diffusion of protons in the xy-plane at different energies. The proton positions are recorded at $t = 400\,\text{years}$, $t = 1000\,\text{years}$ and $t = 7000\,\text{years}$, with time increasing for each row. The energy starts at $E = 1\,\text{PeV}$ in the first column, ending with $E = 1000\,\text{PeV}$ in the rightmost column. Each column increases the energy by a factor of 10. The x- and y-axes are in parsecs, and are scaled with respect to the furthest propagated particles in each direction.

anisotropic behavior at all. There seem to be no apparent filamentary structures. One probable explanation for this, when considering the result shown in figure A.1, is that the transition time might already have passed after 500 years. The protons seem to be transitioning to the isotropic regime already after $t = 50\,\text{years}$. Comparing this with the diffusion coefficients in figure 3.5, 300 years seem to be enough for the lower scale size field to become isotropic.

3.2.3 Transition Time

In sections 3.2.1 and 3.2.2 the behavior of the diffusion protons is discussed, without looking extensively at the time frame. From the intensity plots, Figures 3.6, A.1 and A.2, it is shown that higher energy protons enter the isotropic regime earlier than lower energy particles. The same was also shown in the case where the scale size was decreased. This seems to suggest the transition time decreases when the energy is increased or the scale size is decreased. As the average diffusion coefficient increases with increased energy, it reads from Eq. (2.11.1) that the transition time should increase.

From figure 3.4 the transition time can be seen as the point where diffusion

coefficients begin converging. it is clear from the figure that the anisotropic divergence of the coefficients arise later with higher energy. However, the point on the graphs where the coefficients start converging doesn't seem to change until the highest energy simulated, $E = 1000\,\mathrm{PeV}$.

Seemingly, there is an inconsistency between the results regarding the transition time. One possible reason for this, is that the diffusion time doesn't actually scale as given in Eq. (2.11.1). In the discussion of Giacinti et al. (2012) Figure 2 (figure C.2 in Appendix C) the scaling is said to be $t \propto 1/D(E)$, while the transition time is earlier in the same paper given as in Eq. (2.11.1). A scaling of $t \propto 1/D(E)$ seems more consistent with the behavior shown in the intensity plots both here and in Giacinti et al. (2012), while the behavior expected from equation 2.11.1 is apparent in figure 3.4.

3.2.4 The Average Diffusion Coefficient

From Eq. (2.10.4) the expected average value of the diffusion coefficients can be calculated. This value gives the expected value of the average diffusion coefficient after the CRs have travelled a distance $|\mathbf{r}| \gg L_c$ and have entered the diffusive regime.

Figure 3.8 shows the average diffusion coefficients found from the simulations,

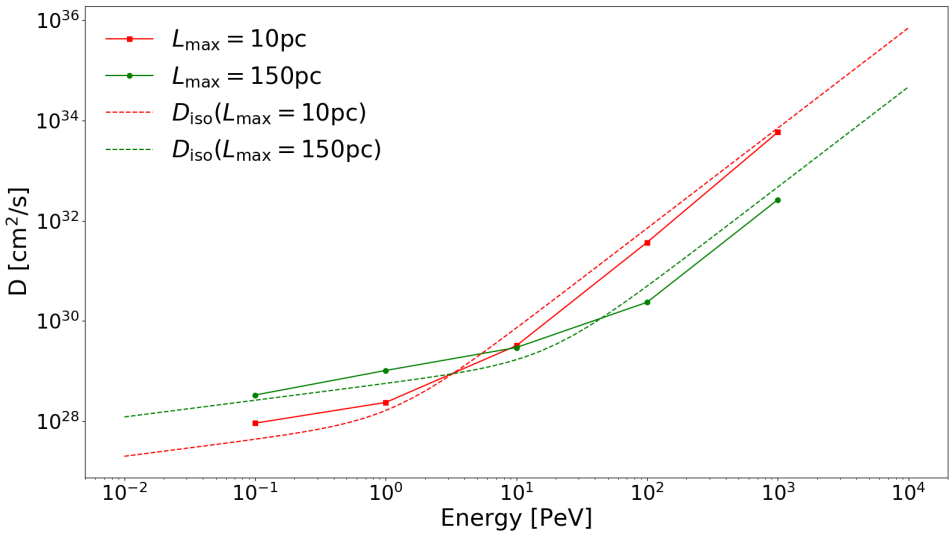

Figure 3.8: Average Diffusion coefficients after the diffusion has entered the isotropic regime, i.e. long after the transition time τ. The simulated energies are given by the solid lines, with the values recorded at the markers.

plotted against the theoretical values given by Eq. (2.10.4). The values for both the theoretical and simulated diffusion coefficients, at the energies of the simulations, are listed in Table 3.2. For both values of $L_{\max}$ the behavior of the simulated values is equivalent to that of the theoretical value. From the behavior seen throughout section 3.2.1 this is expected. One notable difference is how the transformation from $\beta = 1/3$ to $\beta = 2$ occurs. Compared to the theoretical transformation the simulated transformation is slower, i.e. the transformation happens over a longer energy-interval. For $L_{\max} = 150\,\text{pc}$ the transformation starts at approximately $E = 5\,\text{PeV}$ and ends at approximately $E = 40\,\text{PeV}$. The simulated value shows little to no sign of having started transforming at $E = 10\,\text{PeV}$. However, it seems to have transformed when it reaches 100 PeV. The values after the transformations are overall lower for the simulations, while they are higher before the transformation. The same applies for the $L_{\max} = 10\,\text{pc}$ case. The transformation also starts at a slightly higher energy in this case, just as it did for $L_{\max} = 150\,\text{pc}$.

As the behavior of the average diffusion coefficients is equal to that of the theoretical diffusion coefficients, it seems unlikely that there are systematical errors in the simulations. There could be some errors linked to units or constants, although such errors should be independent of the energy and thus contribute a constant error. A more logical explanation would be the numerical accuracy of the simulation. As the turbulent magnetic field is based on a theory where an infinite amount of wave-modes are needed to perfectly produce the turbulence, any finite approximation of this would suffer in accuracy. For these simulation a sufficiently high number of modes have been used, and as such the accuracy should be of a high standard. However, this is just the accuracy of the presentation of the turbulent magnetic field. A numerical error could also be present in the integrator, which in fact is guaranteed to have a certain amount of error. Combining both of these error-sources, it is then expected that there are numerical errors in the results. Based on this it seems reasonable that the majority of the error seen in Figure 3.8 can be accounted to numerical errors.

It could also be argued that the diffusion functional in Eq. (2.10.4) is inaccurate to a certain degree, as it is based on the assumption of the Kolmogorov spectrum. While this could mean that the diffusion functional includes some inaccuracy, the algorithm implemented to calculate the turbulent magnetic field follow the same spectrum. As such, any inaccuracies from the diffusion functional should be equal in the implementation of the turbulent magnetic field.

From the values for the diffusion coefficients given in Table 3.2, the ratio of the theoretical to measured diffusion coefficient can be calculated as $f = D_s/D_t$ where

Table 3.2: List of calculated values for the theoretical diffusion functional D_t given in Eq. (2.10.4), together with the values D_s found from the simulations, long after the transition time.

E[PeV]	$L_{\max}$[pc]	L_0[pc]	R_g[pc]	D_{f}[cm^2/y]	D_{m}[cm^2/y]
1	10	0.32	0.27	$1.54 \cdot 10^{28}$	$2.37 \cdot 10^{28}$
10	10	0.32	2.73	$7.93 \cdot 10^{29}$	$3.22 \cdot 10^{29}$
100	10	0.32	27.25	$7.18 \cdot 10^{31}$	$3.71 \cdot 10^{31}$
1000	10	0.32	272.52	$7.10 \cdot 10^{33}$	$5.87 \cdot 10^{33}$
1	150	4.77	0.27	$5.71 \cdot 10^{28}$	$1.03 \cdot 10^{29}$
10	150	4.77	2.73	$1.31 \cdot 10^{29}$	$2.96 \cdot 10^{29}$
100	150	4.77	27.25	$5.55 \cdot 10^{30}$	$2.37 \cdot 10^{30}$
1000	150	4.77	272.52	$4.80 \cdot 10^{32}$	$2.64 \cdot 10^{32}$

D_s is the simulated value and D_t. Using $L_{\max} = 150\,\mathrm{pc}$ this ratio is calculated to

$$\begin{aligned} f(E = 1\,\mathrm{PeV}) &= 1.78, \\ f(E = 10\,\mathrm{PeV}) &= 2.25, \\ f(E = 100\,\mathrm{PeV}) &= 0.43, \\ f(E = 1000\,\mathrm{PeV}) &= 0.55 \end{aligned}$$

To look at the relative difference, it is interesting to compare the inverse of the two latter values to the two first values. This gives

$$\begin{aligned} f(E = 1\,\mathrm{PeV}) &= 1.78, \\ f(E = 10\,\mathrm{PeV}) &= 2.25, \\ f^{-1}(E = 100\,\mathrm{PeV}) &= 2.33, \\ f^{-1}(E = 1000\,\mathrm{PeV}) &= 1.82 \end{aligned}$$

which gives an indication that during the transformation the values differ slightly more than they do before and after the transformation happens. However, in all three regimes the values differ within reason of numerical errors.

Comparing the behavior and values to Figure 1 from Giacinti et al. (2018) (Figure C.4 in Appendix C), both the values and behavior are in close agreement with the expected values. The closest magnetic field value from Giacinti et al. (2018) to the values used for this report, are the yellow points which uses $B = 5\,\mu\mathrm{G}$ and $L_{\max} = 25\,\mathrm{pc}$. Since the value used here is $B = 4\,\mu\mathrm{G}$ and $L_{\max} = 10\,\mathrm{pc}$, the transformation is expected to happen approximately at the same energies. Comparing Figure C.4 to Figure 3.8, it is found that both transformations starts at approximately $E = 0.2\,\mathrm{PeV}$ and ends at approximately $E = 4\,\mathrm{PeV}$.

While there are still some numerical errors in the simulation of the diffusion of the CRs, the behavior and amplitudes of the diffusion coefficients are well within acceptable ranges.

CHAPTER 4

HAMILTONIAN GUIDING CENTER THEORY

Hamiltonian GCT derives the EoM of the guiding center using the Lagrangian and Hamiltonian formalisms. Applied to charged particles in electromagnetic fields, it will under certain assumptions describe the trajectories of the guiding center through the particles helical movement about the magnetic field lines. This chapter will closely follow Cary and Brizard (2009) Ch. II and II.

Lagrangian and Hamiltonian formalism

The Euler-Lagrange equations are given on their general form as

$$\frac{d}{dt}\left(\frac{\partial L}{\partial \dot{q}^i}\right) = \frac{\partial L}{\partial q^i} \tag{4.1.1}$$

where q are the generalized coordinates and $\dot{q}$ are the time-derivatives. For a charged particle in an electromagnetic field the Lagrangian is given, in Cartesian coordinates, as

$$L = \frac{m}{2}|\dot{\mathbf{x}}|^2 + q\,\dot{\mathbf{x}} \cdot \mathbf{A}\left(\mathbf{x}, t\right) - q\,\Phi\left(\mathbf{x}, t\right) \tag{4.1.2}$$

(Cary and Brizard, 2009, ch. II-A). Here $\mathbf{A}$ is the vector potential and Φ the electric field potential, giving the electromagnetic field as

$$\mathbf{E} = -\nabla\Phi - \frac{\partial \mathbf{A}}{\partial t}, \tag{4.1.3}$$

$$\mathbf{B} = \nabla \times \mathbf{A} \tag{4.1.4}$$

(Griffiths, 2013, p. 416-417). Going forward the derivation of the GC EoM will follow Cary and Brizard (2009), Ch. II and III, using SI-units instead of cgs-units.

This leads to some factors of c being left out in the equations given in this paper, compared to the equations in Cary and Brizard (2009).

The Lagrangian formalism is coordinate independent, meaning the action integral

$$A[\mathbf{x}] = \int L\left(\mathbf{x}, \dot{\mathbf{x}}; t\right) dt \tag{4.1.5}$$

can be calculated in any coordinate system. Allowed trajectories of the Lagrangian satisfy the statement $\partial A = 0$, which can be stated without reference to any certain coordinate system. To transform from the Lagrangian in Eq. (4.1.2) to the general coordinates $\mathbf{q}$, the substitutions

$$\mathbf{x} \rightarrow \mathbf{x}\left(\mathbf{q}, t\right), \tag{4.1.6}$$

$$\dot{\mathbf{x}} = \frac{\partial \mathbf{x}}{\partial t} + \sum \dot{q}^i \frac{\partial \mathbf{x}}{\partial q^i} \tag{4.1.7}$$

are applied. Now Eq. (4.1.1) can be expressed in the desired, convenient coordinates of choice. Furthermore, the canonical momentum $\mathbf{p}$ can be defined as

$$p_i = \frac{\partial L}{\partial \dot{q}^i}\left(\mathbf{q}, \dot{\mathbf{x}}, t\right) \tag{4.1.8}$$

with p_i being the individual components. Whenever Eq. (4.1.8) can be inverted to find the velocities as functions of the canonical momenta, $\dot{q}^i\left(\mathbf{q}, \mathbf{p}, t\right)$, Hamiltonian formalism may be used. In this formalism points in phase space is determined by $\mathbf{q}$ and $\mathbf{p}$ instead of $\mathbf{q}$ and $\dot{\mathbf{q}}$. The Hamiltonian is defined through the Legendre transformation as

$$H\left(\mathbf{q}, \mathbf{p}, t\right) = \mathbf{p} \cdot \dot{\mathbf{q}}\left(\mathbf{q}, \mathbf{p}, t\right) - L\left[\mathbf{q}, \dot{\mathbf{q}}\left(\mathbf{q}, \mathbf{p}, t\right), t\right] \tag{4.1.9}$$

and the EoM are Hamilton's equations

$$\dot{q}^i = \frac{\partial H}{\partial p_i}, \tag{4.1.10}$$

$$\dot{p}_i = -\frac{\partial H}{\partial q^i}. \tag{4.1.11}$$

In Cartesian coordinates, for a charged particle in an electromagnetic field, the corresponding Hamiltonian is

$$H\left(\mathbf{x}, \mathbf{p}, t\right) = \frac{1}{2m}\left|\mathbf{p} - q\mathbf{A}\left(\mathbf{x}, t\right)\right|^2 + q\Phi\left(\mathbf{x}, t\right) \tag{4.1.12}$$

with the canonical momenta from Eq. (4.1.8) $p_i = m\dot{x}_i + qA_i$.

Noncanonical Guiding-Center Lagrangian

In the Lagrangian formalism it is possible to make arbitrary coordinate transformations. A Lagrangian that gives the correct EoM when all phase-space coordinates is varied, is called the phase-space Lagrangian $\mathcal{L}$. It has the same value as the Lagrangian L, and can be defined from Eq. (4.1.9) as

$$\mathcal{L}\left(\mathbf{q},\mathbf{p},\dot{\mathbf{q}},\dot{\mathbf{p}},t\right) \equiv \mathbf{p}\cdot\dot{\mathbf{q}} - H\left(\mathbf{q},\mathbf{p},t\right). \tag{4.2.1}$$

Inserting Eq. (4.1.12) into Eq. (4.2.1), the phase-space Lagrangian

$$\mathcal{L} = \mathbf{p}\cdot\dot{\mathbf{x}} - \frac{1}{2m}\left|\mathbf{p} - q\mathbf{A}\left(\mathbf{x},t\right)\right|^2 - q\Phi\left(\mathbf{x},t\right) \tag{4.2.2}$$

for a particle moving in an electromagnetic field. Defining the particle velocity $\mathbf{v} \equiv \frac{1}{m}\left(\mathbf{p} - q\mathbf{A}\right)$, the phase-space Lagrangian for the noncanonical variables $(\mathbf{x},\mathbf{v})$

$$\mathcal{L} = \left(m\mathbf{v} + q\mathbf{A}\right)\cdot\dot{\mathbf{x}} - \left(q\Phi + \frac{m}{2}|\mathbf{v}|^2\right) \tag{4.2.3}$$

is found. Solving the Euler-Lagrange equation for $\mathcal{L}$ with respect to $\mathbf{v}$ gives the identity $\mathbf{v} = \dot{\mathbf{x}}$. Solving Eq. (4.1.1) with respect to $\mathbf{x}$ yields

$$m\dot{\mathbf{v}} = q\mathbf{E} + q\mathbf{v}\times\mathbf{B}, \tag{4.2.4}$$

which is recognized as the Lorentz force on a charged particle.

To derive a Lagrangian for the GC a transformation to alternative phase-space coordinates is sought, where the degree of freedom corresponding to the gyromotion is absent in the EoM. The transformation is found assuming the gyroradius is small, and the field is slowly varying. An ordering parameter ϵ is applied to the Lagrangian in Eq. (4.2.3) such that $q/m \equiv \epsilon^{-1} = \Omega/B$. The ordered Lagrangian then becomes

$$\mathcal{L}\left(\mathbf{x},\mathbf{v},t\right) = \left(\epsilon^{-1}\mathbf{A}\left(\mathbf{x},t\right) + \mathbf{v}\right)\cdot\dot{\mathbf{x}} - \left(\frac{1}{2}|\mathbf{v}|^2 + \epsilon^{-1}\Phi\left(\mathbf{x},t\right)\right). \tag{4.2.5}$$

The ordering parameter is chosen such that in the limit when ϵ is small, the electromagnetic field dominates, as the kinetic energy terms are of order 1 with respect to ϵ. Evaluating the lowest order motion, the $\mathcal{O}\left(\epsilon^{-1}\right)$ terms are kept giving the lowest-order Lagrangian $\mathcal{L}_{-1} \equiv \mathbf{A}\cdot\dot{\mathbf{x}} - \Phi$. Solving the Euler-Lagrange equation for $\mathcal{L}_{-1}$ gives

$$\dot{\mathbf{x}}\times\mathbf{B} + \mathbf{E} = \mathbf{0} \tag{4.2.6}$$

which determines that the perpendicular velocity is equal to the electric drift, i.e. $\dot{\mathbf{x}}_\perp = \mathbf{v}_E$. A transformation of the position variable on the form

$$\mathbf{x} = \mathbf{X} + \epsilon\boldsymbol{\rho} \tag{4.2.7}$$

is expected to work. Here $\mathbf{x}$ is the coordinate of the particle, $\mathbf{X}$ is the GC coordinate and $\boldsymbol{\rho}$ is the gyroradius displacement. The displacement vector is defined as $\boldsymbol{\rho} \equiv \tilde{\boldsymbol{\rho}} + \bar{\boldsymbol{\rho}}$ where $\tilde{\boldsymbol{\rho}}$ is explicitly dependent on the gyrophase ζ and $\bar{\boldsymbol{\rho}}$ is gyrophase independent. To apply the transformation in Eq. (4.2.7) to the Lagrangian, the time derivative

$$\dot{\mathbf{x}} = \dot{\mathbf{X}} + \dot{\boldsymbol{\rho}} \tag{4.2.8}$$

is needed. Here

$$\dot{\boldsymbol{\rho}} = \dot{\zeta}\frac{\partial \tilde{\boldsymbol{\rho}}}{\partial \zeta} + \epsilon\left(\mathbf{v}\cdot\nabla\tilde{\boldsymbol{\rho}} + \dot{\bar{\boldsymbol{\rho}}}\right) = \frac{\mathbf{w}}{B}\dot{\zeta} + \mathcal{O}(\epsilon) \tag{4.2.9}$$

where $\mathbf{w} = \mathbf{v}_\perp - \mathbf{v}_E$ is the perpendicular velocity in the local frame drifting with $\mathbf{E}\times\mathbf{B}$. Using Eq. (4.2.7) and Eq. (4.2.8) to expand the field quantities $(\mathbf{A}, \Phi)$ to the zeroth order, inserting it into Eq. (4.2.5) gives

$$\begin{aligned}\mathcal{L} = \ & \epsilon^{-1}\left[\mathbf{A}\cdot\left(\dot{\mathbf{X}} + \dot{\boldsymbol{\rho}}\right) - \Phi\right] + \boldsymbol{\rho}\cdot\left[\nabla\cdot\mathbf{A}\cdot\left(\dot{\mathbf{X}} + \dot{\boldsymbol{\rho}}\right) - \nabla\Phi\right] \\ & + \mathbf{v}\cdot\left(\dot{\mathbf{X}} + \dot{\boldsymbol{\rho}}\right) - \tfrac{|\mathbf{v}|^2}{2} + \mathcal{O}(\epsilon)\,.\end{aligned} \tag{4.2.10}$$

From this point $(\mathbf{A}, \Phi)$ are evaluated at the GC position $\mathbf{X}$, with the gradient also taken with respect to $\mathbf{X}$.

To remove the gyrophase-dependence of the Lagrangian in Eq. (4.2.10), the second term $\epsilon^{-1}\mathbf{A}\cdot\dot{\boldsymbol{\rho}}$ needs to be pushed to a higher order. Excluding the exact time derivative in the expansion and excluding terms of $\mathcal{O}(\epsilon)$, Eq. (4.2.10) becomes

$$\mathcal{L} = \epsilon^{-1}\left(\mathbf{A}\cdot\dot{\mathbf{X}} - \Phi\right) + \boldsymbol{\rho}\cdot\left(\mathbf{E} + \dot{\mathbf{X}}\times\mathbf{B}\right) + \boldsymbol{\rho}\cdot\nabla\mathbf{A}\cdot\dot{\boldsymbol{\rho}} + \mathbf{v}\cdot\left(\dot{\mathbf{X}} + \dot{\boldsymbol{\rho}}\right) - \frac{|\mathbf{v}|^2}{2}. \tag{4.2.11}$$

Using the exact derivative of the third term, still excluding terms of $\mathcal{O}(\epsilon)$, the Lagrangian is written as

$$\mathcal{L} = \epsilon^{-1}\left(\mathbf{A}\cdot\dot{\mathbf{X}} - \Phi\right) + \boldsymbol{\rho}\cdot\left(\mathbf{E} + \dot{\mathbf{X}}\times\mathbf{B}\right) + \frac{1}{2}\boldsymbol{\rho}\times\dot{\boldsymbol{\rho}}\cdot\mathbf{B} + \mathbf{v}\cdot\left(\dot{\mathbf{X}} + \dot{\boldsymbol{\rho}}\right) - \frac{|\mathbf{v}|^2}{2}. \tag{4.2.12}$$

The terms $\boldsymbol{\rho}\cdot\left(\mathbf{E} + \dot{\mathbf{X}}\times\mathbf{B}\right)$ are representative of the electric dipole contribution to the GC polarization and magnetization respectively. Furthermore, the latterly derived term $\frac{1}{2}\boldsymbol{\rho}\times\dot{\boldsymbol{\rho}}\cdot\mathbf{B}$ describes the intrinsic magnetic dipole contribution to the GC magnetization. Introducing the transformation

$$\boldsymbol{\rho} \equiv \tilde{\boldsymbol{\rho}} + \bar{\boldsymbol{\rho}} = \hat{b}\times\frac{\mathbf{w}}{B} + \frac{\mathbf{E}_\perp}{B^2} \tag{4.2.13}$$

where $\hat{b}$ is the magnetic field unit vector, defining the GC velocity $u \equiv v_{\parallel} + \mathcal{O}(\epsilon)$, and using $\tilde{\boldsymbol{\rho}} \cdot \mathbf{E} = \mathbf{w} \cdot \mathbf{v}_E$ as well as $\bar{\boldsymbol{\rho}} \cdot \mathbf{E} = |\mathbf{v}_E|^2$, the ordered phase-space Lagrangian can be written as

$$\mathcal{L} = \left(\epsilon^{-1}\mathbf{A} + u\hat{b}\right) \cdot \dot{\mathbf{X}} + \left(\frac{|\mathbf{w}|^2}{2B} + \mathbf{v}_E \cdot \frac{\mathbf{w}}{2B}\right)\dot{\zeta} - \left(\epsilon^{-1}\Phi + \frac{u^2}{2} + \frac{|\mathbf{w}|^2}{2} - \frac{|\mathbf{v}_E|^2}{2}\right). \tag{4.2.14}$$

Finally, subtracting the total time derivative of the last $\mathcal{O}(1)$ gyrophase-dependent term, $\mathbf{v}_E \cdot (\mathbf{w}/2B)\dot{\zeta}$, and omitting all terms of $\mathcal{O}(\epsilon)$, the dimensionless GC Lagrangian

$$\mathcal{L} = \left(\epsilon^{-1}\mathbf{A} + u\hat{b}\right)\dot{\mathbf{X}} + J\dot{\zeta} - H_{\mathrm{gc}} \equiv \mathcal{L}(\mathbf{X}, u, \mu, \zeta, t) \tag{4.2.15}$$

is found. Here the gyroaction is defined as $J \equiv w^2/2B$, and the GC Hamiltonian is

$$H_{\mathrm{gc}}(\mathbf{X}, u, \mu, \zeta, t) = \epsilon^{-1}\Phi + J\Omega + \frac{u^2}{2} - \frac{|\mathbf{v}_E|^2}{2}. \tag{4.2.16}$$

Guiding Center Equations of Motion

In summary of section 4 the essential new variables are the GC position $\mathbf{X}$, the GC velocity u and the gyrophase ζ. In Eq. (4.2.15) $\mathcal{L}$ is given as a function of μ, where

$$\mu \equiv \frac{m|w|^2}{2B} \tag{4.3.1}$$

defines the lowest-order magnetic moment. It is linked to the gyroaction by $J \equiv (m/q)\mu$. The Hamilton equations for J and ζ are

$$\dot{J} = -\frac{\partial H_{\mathrm{gc}}}{\partial \zeta} \equiv 0, \tag{4.3.2}$$

$$\dot{\zeta} = \frac{\partial H_{\mathrm{gc}}}{\partial J} \equiv \Omega. \tag{4.3.3}$$

This shows that the gyroaction is conserved by the GC EoM. While μ appears in the EoM, it is only a dynamical parameter and not an actual variable. As only the time derivative of ζ appears in the EoM, and because it is constant, it can be ignored in the GC Lagrangian as it does not affect the EoM of the other variables.

Solving Eq. (4.1.1) with respect to u

$$0 = \frac{\partial \mathcal{L}}{\partial u} = m\hat{b} \cdot \dot{\mathbf{X}} - \frac{\partial H_{\mathrm{gc}}}{\partial u}, \tag{4.3.4}$$

which gives

$$u \equiv \hat{b}(\mathbf{X}, t) \cdot \dot{\mathbf{X}}. \tag{4.3.5}$$

Next solving Eq. (4.1.1) with respect to $\mathbf{X}$ and manipulating it in the same manner as for Eq. (4.2.3) to find Eq. (4.2.4),

$$\begin{aligned} m\dot{u}\hat{b} &= q\mathbf{E} - \mu\nabla B + \frac{m}{2}\nabla|\mathbf{v}_E|^2 - mu\frac{\partial\hat{b}}{\partial t} + \dot{\mathbf{X}}\times\left(q\mathbf{B} + mu\nabla\times\hat{b}\right) \\ &\equiv q\left(\mathbf{E}^* + \dot{\mathbf{X}}\times\mathbf{B}^*\right). \end{aligned} \tag{4.3.6}$$

Here the effective electromagnetic fields

$$\mathbf{E}^* \equiv -\nabla\Phi^* - \frac{\partial\mathbf{A}^*}{\partial t} \tag{4.3.7}$$

and

$$\mathbf{B}^* \equiv \nabla\times\mathbf{A}^* \tag{4.3.8}$$

are defined in terms of the effective electromagnetic potentials

$$q\Phi^* \equiv q\Phi + \mu B - \frac{m}{2}|\mathbf{v}_E|^2 \tag{4.3.9}$$

and

$$\mathbf{A}^* \equiv \mathbf{A} + \frac{mu}{q}\hat{b}. \tag{4.3.10}$$

To find the rate of change of u, the dot product of Eq. (4.3.6) with $\mathbf{B}^*$ is taken, yielding

$$\dot{u} = -\frac{\mathbf{B}^*}{mB_\parallel^*}\cdot\left(\nabla H_{\rm gc} + q\frac{\partial\mathbf{A}^*}{\partial t}\right) \equiv \frac{q}{m}\frac{\mathbf{B}^*}{B_\parallel^*}\cdot\mathbf{E}^*, \tag{4.3.11}$$

where $B_\parallel^* \equiv \hat{b}\cdot\mathbf{B}^*$ is the effective magnetic field in the direction parallel to $\mathbf{B}^*$.

Finally the GC velocity is found by taking the vector product of Eq. (4.3.6) with $\hat{b}$ and using Eq. (4.3.5) to get

$$\begin{aligned} \dot{\mathbf{X}} &= \frac{\mathbf{B}^*}{mB_\parallel^*}\frac{\partial H_{\mathbf{gc}}}{\partial u} + \frac{\hat{b}}{mB_\parallel^*}\times\left(\nabla H_{\mathbf{gc}} + q\frac{\partial\mathbf{A}^*}{\partial t}\right) \\ &= u\frac{\mathbf{B}^*}{B_\parallel^*} + \mathbf{E}^*\times\frac{\hat{b}}{B_\parallel^*}. \end{aligned} \tag{4.3.12}$$

Eqs. (4.3.11) and (4.3.12) constitutes the EoM for the GC, and are in principle the only equations needed to find the trajectories of the GC. In addition, Eq. (4.3.3) is needed if the particle position along the helix is wanted.

CHAPTER 5

NUMERICAL IMPLEMENTATION OF THE GUIDING CENTER THEORY

In the following chapter the implementation of the GC EoM in a numerical solver is described, along with the results of the simulations performed using this implementation. The code for this project was written in C++. The integrator and RNG were taken from Press et al. (2007). All other code, as well as the modifications to the integrator, was written by the author of this report. The complete code can be found at Github.com/odde92/master_thesis. It is worth noting that all vector values, e.g. $\mathbf{v}$, are programmed as arrays with 3 values, where the values are stored component-wise as $\mathbf{A} = \{A_x, A_y, A_z\}$.

Implementation of the Guiding Center Equations of Motion

5.1.1 Initialization

To make comparing the GC trajectory to the exact trajectory easy, the GC is initialized using the same particle that would be used in the exact solution. In this program the energy and type of particle, as well as the starting position, is chosen before running the simulation. As such it is only the direction of the particle's velocity that is randomly generated at run-time. After initializing the particle in the same manner as described in section 3.1.2, the magnetic field is initialized and calculated at the particle's starting position. Then, using

$$\dot{\mathbf{X}} = \dot{\mathbf{x}} \cdot \hat{b} \tag{5.1.1}$$

as the initial condition, the GC velocity is set.

Finding the GC starting position now becomes a 5-step process. First the amplitude of the particle's velocity perpendicular to $\hat{b}$ is calculated. The initial condition for the GC velocity is chosen as $\left|\dot{\mathbf{X}}\right| = v_\parallel$, such that the perpendicular velocity can be found by $v_\perp = \sqrt{v^2 - v_\parallel^2}$. With $v_\perp$ calculated, the Larmor radius can be found using (2.9.2). The third step is to calculate

$$\mathbf{v}_\perp = \mathbf{v} - \mathbf{v}_\parallel. \tag{5.1.2}$$

As $\mathbf{v}_\parallel$ is aligned with $\hat{b}$, and $\mathbf{v}$ is initialized with the particle, $\mathbf{v}_\perp$ is known. Next, the vector pointing from the particle's position towards the center of the helix is defined as $\mathbf{a} = \mathbf{v}_\perp \times \hat{b}$, and the normalized vector is $\hat{a} = \mathbf{a}/a$. The final step is to take a step of length R_L in the direction of $\hat{a}$,

$$\mathbf{X} = R_L \cdot \hat{a}. \tag{5.1.3}$$

5.1.2 Guiding Center Propagation

After completing the initialization of the GC, the integrator has to be initialized. This only requires the initial-values calculated in section 5.1.1. After setting the initial values, the integrator-object is created, taking the magnetic field, particle and GC as members. When the integrator-object has been initialized, it is passed to the integrator itself. The integrators from Press et al. (2007) enables easy swapping of integrators, and the integration method used to generate the results of this report is the Bulirsch-Stoer RK method. This is a step-size controlling integration method, meaning it will decide on a proper time-step given an error-tolerance threshold.

The RK methods use several substeps to perform one step in the integration. At each of these substeps the integrator calls a function from the integrator-object to calculate the derivative values. The derivates needed are the ones from Eqs. (4.3.11) and (4.3.12). At each substep several calculations are needed to find the derivative values used in the equation. First the magnetic field and $\hat{b}$ at the substep is calculated. After this $\partial_i \hat{b}$ is calculated for $i \in (x, y, z)$, using a first-order forward difference scheme. The step size of the differential is calculated using $h = u \cdot \Delta t$, where Δt is the time-step decided by the integrator. Now the effective fields $\mathbf{E}^*$ and $\mathbf{B}^*$ can be calculated.

The effective electric field $\mathbf{E}^*$ is calculated assuming μ is a constant at each point. Inserting this into Eq. (4.3.7), inserting Eq. (4.3.9) and using $\mathbf{E} = 0 \implies \{\mathbf{v}_E = 0, \Phi = 0\}$,

$$\mathbf{E}^* = -\frac{\mu}{q}\nabla B \tag{5.1.4}$$

Table 5.1: List of variables, and their units, used in the simulation of the guiding center trajectories in the Galactic magnetic field.

Parameter	Unit	Description
$\mathbf{X}$	pc	In/output GC position
$\boldsymbol{\mathcal{X}}$	m	GC position during integration
$\dot{\boldsymbol{\mathcal{X}}}$	$\mathrm{m\,s^{-1}}$	GC velocity during integration
u	$\mathrm{m\,s^{-1}}$	GC velocity in $\hat{b}$-direction
m	$\mathrm{MeV/c^2}$	CR mass
q	e	CR charge
B_0	µG	Coherent magnetic field strength
B_{rms}	µG	turbulent magnetic field RMS strength
$\mathbf{B}^*$	µG	Effective magnetic field
$\mathbf{E}^*$	$\mathrm{V\,m^{-1}}$	Effective electric field

gives the three equations for the effective electric field. From Eqs. (4.3.8) and (4.3.10), the effective magnetic field

$$\mathbf{B}^* = \mathbf{B} + \frac{m}{q}\nabla \times u\hat{b} \tag{5.1.5}$$

is found. To calculate the last term, the identity $\nabla \times u\hat{b} = u\left(\nabla \times \hat{b}\right) + (\nabla u) \times \hat{b}$ is used to break the equation into parts that are possible to calculate. $\nabla \times \hat{b}$ is known as $\partial_i \hat{b}$ is already determined. Finding ∇u is done using Eq. (4.3.5) and the fact that $\nabla \dot{\mathbf{X}} = 0$, giving

$$\nabla u = \sum_i \left(\dot{\mathbf{X}} \cdot \partial_i \hat{b}\right) \hat{i} \tag{5.1.6}$$

with $i \in (x, y, z)$. With $\mathbf{E}^*$, $\mathbf{B}^*$ and $\hat{b}$ determined, Eq. (4.3.12) can be implemented after calculating $\mathbf{E}^* \times \hat{b}$. The last EoM to solve is Eq. (4.3.11), which is dependent on $\mathbf{B}^* \cdot \mathbf{E}^*$. Both fields are of course known, effectively solving the equation.

With all parts in the EoM determined, they are then implemented in the integrator-object and passed to the integrator. The output is saved after each step calculated by the integrator and written to a file at the end of the integration. This sets a limit for the number of steps possible to take, based on how much memory is available. However, any trajectories with that many steps is most likely using an error tolerance that is too low, or is being run for an exceedingly long period of time.

5.1.3 Units

Keeping track of the correct units can be cumbersome. In the code for this project the integration is done in SI-units. However, the input is taken in more convenient units, and conversion coefficients are needed in the EoM. Table 5.1 lists the variables used, and what units they were given in the program. Due to the nature of the equations, inserting the conversion coefficient is quite cumbersome compared to the units in the exact solution. In table 5.2 the conversion units are listed. For the GC velocity, Eq. (4.3.12), the magnetic field units cancel and the unit of the first term is the unit of u, $\mathrm{m\,s^{-1}}$. In the second term $\mathbf{E}^*$ has units $\mathrm{V\,m^{-1}}$, while $B^*_\parallel$ has unit µG. To get this in $\mathrm{m\,s^{-1}}$ as for the first term, µG is converted to Tesla.

All equations where either m/q or q/m appears, the equation is multiplied with the $\mathrm{kg/C} \to \mathrm{MeV/c^2e}$ conversion coefficient or its inverse. Whenever q appears by itself the conversion coefficient for Coulomb to Elementary charge is used. Finally meter to parsec is used on the initial position, and parsec to meter is used when converting the output of the integrator to the final output of the program.

Table 5.2: Conversion coefficients between the input and integration parameters used in the program.

Conversion coefficient	Value	Description
$\mathrm{m} \to \mathrm{pc}$	$3.240\,78 \cdot 10^{-17}$	Meter to Parsec
$\mathrm{pc} \to \mathrm{m}$	$3.085\,68 \cdot 10^{16}$	Parsec to Meter
$\mu\mathrm{G} \to \mathrm{T}$	$1 \cdot 10^{10}$	Microgauss to Tesla
$\mathrm{C} \to e$	$6.241\,51 \cdot 10^{18}$	Coulomb to Elementary Charge
$\mathrm{kg/C} \to \mathrm{MeV/c^2e}$	$1.165\,80 \cdot 10^{-11}$	Mass per Charge coefficient

Results of Guiding Center Simulations

To test the implementation of the Hamiltonian GCT, different tests were run using different magnetic fields. The first step in testing the Hamiltonian GCT was to apply it to simulations of CRs in a uniform field with constant field strength. If this succeeded, the theory could then be implemented in more complex fields, such as a spiral field and a uniform field in superposition with a turbulence. Table 5.3 lists the static variables used during the simulations. These variables are used for all Figures throughout this chapter unless it is otherwise stated in the Figure text.

Table 5.3: List of static parameters used in the simulation of the Guiding Center trajectories in the Galactic magnetic field.

Parameter	Value	Unit	Description
m	938.2720813	$\mathrm{MeV/c^2}$	Proton mass
q	1	$1.602 \cdot 10^{-19}\,\mathrm{C}$	Charge in # of elementary charges
B_0	10.0	µG	Coherent magnetic field strength
B_{rms}	$\%B_0$	µG	TMF RMS strength
L_{max}	150	pc	Max TMF scale size
N	100	-	# of Fourier modes in TMF
t	5000	years	Runtime of simulations
(x_0, y_0, z_0)	$(100, 100, 0)$	pc	Particle initial position
rtol	$1 \cdot 10^{-16}$	-	Relative error tolerance
atol	$1 \cdot 10^{-16}$	-	Absolute error tolerance

5.2.1 Uniform Field

The first test was to check that the implementation gave the expected result for the uniform field. Eq. (5.1.4) immediately gives that $\mathbf{E}^* = \mathbf{0}$ for this field. From Eqs. (5.1.6) and (5.1.5) the effective magnetic field becomes $\mathbf{B}^* = \mathbf{B}$. Thus, the EoM for the uniform, constant field strength magnetic field becomes

$$\dot{\mathbf{X}} = u\mathbf{B} \tag{5.2.1}$$

$$\dot{u} = 0. \tag{5.2.2}$$

This is the equation for a straight line, which is as expected in this field configuration. Implementing the equations in the field will not only test if the equations hold in the trivial case, but it will simultaneously test that the initial condition $u_0 = v_{\parallel,0}$ holds.

In Figure 5.1 the resulting trajectories are seen. This shows that the initial condition for u holds. It also shows that the calculation of the initial GC-position works, given a particle with an initial position and velocity.

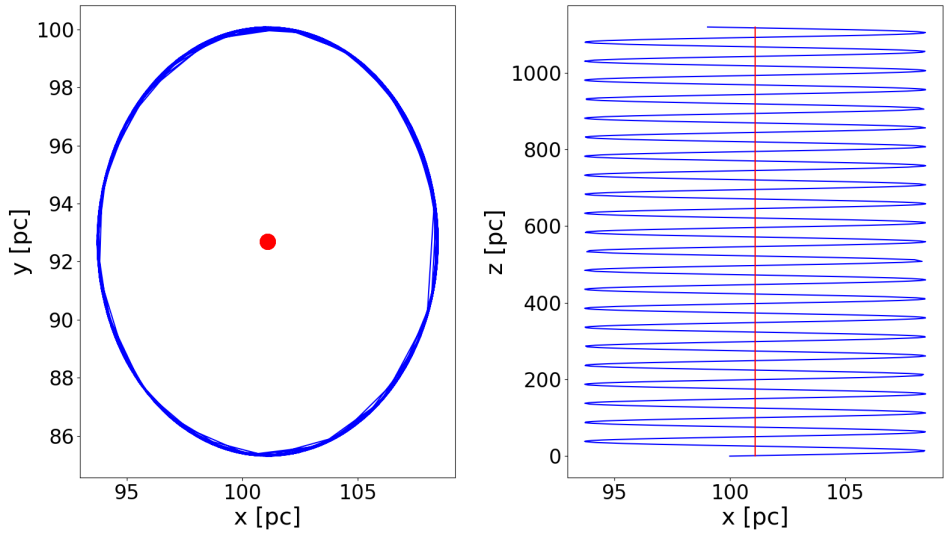

Figure 5.1: Comparison between the exact solution, plotted as a blue line, and the GC solution, plotted as a red line, in a uniform field $\mathbf{B} = B_0\hat{z}$. For this simulation $E = 100\,\text{PeV}$ was used for the CR.

From the view of the xy-plane it is seen that the GC stays centered throughout the whole simulation. The position of the GC is also found to be well centered in the helix. As the starting position of the particle is $\mathbf{r}_0 = (100, 100, 0)$, it seems a bit odd that the GC isn't centered on 100 pc on either axis. This can be explained by the fact that velocity of the particle is randomly chosen, uniformly on a sphere. Thus, the GC initial position is skewed to fit the direction the CR travels initially.

5.2.2 Spiral Field with Constant Field Strength

Continuing with a field of constant field strength, the next step is to introduce a curl. One way of doing this is to generate a magnetic field on the form

$$\mathbf{B} = [\sin(\theta)\cos(\phi) - \cos(\theta)\sin(\phi)]\,\hat{x} + [\sin(\theta)\sin(\phi) + \cos(\theta)\cos(\phi)]\,\hat{y} \qquad (5.2.3)$$

where $\theta = 11.5^\circ\frac{\pi}{180}$ and $\phi = \arctan(y/x)$. The value of θ is chosen such that the spiral magnetic field roughly resembles the spirals of the Milky Way. However, the proper representation of the Galactic magnetic field is also dependent on a factor $B(\rho, \phi)$ which has been set to $B(\rho, \phi) = B_0$ for these simulations.

In a spiral magnetic field the effects of the gradient leads to an acceleration of the particle along the magnetic field lines. This means $v_{\parallel}$ will increase in the direction of $\hat{b}$. For a particle initially travelling in the opposite direction of the magnetic field line, this results in a retardation, and eventually a reflection of the particle. Figure 5.2 shows the simulation of a proton with an initial velocity opposite to the magnetic field line. The exact solution shows an apparent gradient effect affecting the trajectory. While there is no gradient in the field, as the magnetic field strength is constant, there is a divergence in the field. From Maxwell's equation it is given that $\nabla \cdot \mathbf{B} = 0$, meaning the applied spiral field is not a real magnetic field. Having a divergence in the field is analogous to introducing magnetic monopoles. This would again lead to a magnetic potential field analogous to the electric potential field. Since the particle is propagated through this field, which now has a magnetic potential, it will experience the same effects as if it was propagating in a magnetic field with a gradient, where it is accelerated in the direction of $\hat{b}$ (Shnir, 2006, Ch. 1).

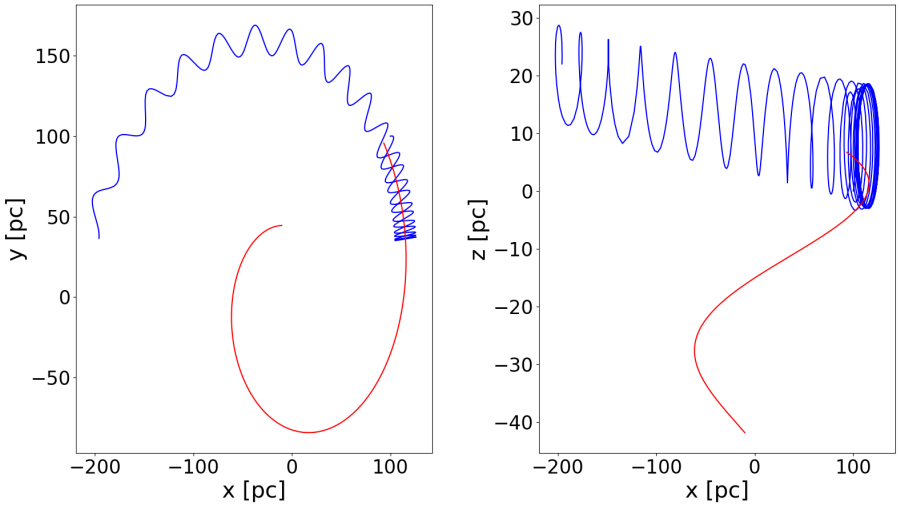

Figure 5.2: Simulation of a CR with an initial parallel velocity in the opposite direction of the magnetic field line. The exact solution is plotted in blue, while the GCT solution is plotted in red. In this simulation the CR used was a proton with $E = 100\,\mathrm{PeV}$.

On the other hand, the GCT solution never decelerates, and continues inwards along the magnetic field line at a constant speed. Checking the value of the GC parallel velocity and its derivative, $\dot{u}$ is found to be 0. As the assumption of μ being constant is made, Eq. (5.1.4) immediately gives $\mathbf{E}^* = 0$ for all magnetic fields with a constant field strength, which in turn determines that $\dot{u} = 0$. While

$\mathbf{E}^*$ is zero, $\mathbf{B}^*$ is not. Eq. (5.1.5) also determines that $\mathbf{B}^* \neq \mathbf{B}$, as $\partial_i \hat{b}$ is not zero for ∂_x and ∂_y. The difference in propagated distance between the exact solution and the GC solution is therefore attributed to the choice of a divergent magnetic field.

Simulating the same CR with an initial parallel velocity in the same direction as $\hat{b}$ gives the result shown in Figure 5.3. The lack of an acceleration in the parallel direction is still evident. At the same time the particle follows nicely through the center of the helix made by the exact solution, as seen from the projection onto the xy-plane. When projected onto the xz-plane the effects of the curl is clearly seen. As expected from the drift velocity in Eq. (2.8.5) the particle drifts in the $\hat{z}$-direction. In Figure 5.2 the GC drifts in the $-\hat{z}$-direction, which is expected when the particle propagates in the opposite direction of the magnetic field. Figures 5.3 and A.4 show that the drift-velocity is constant for the GC, while it depends on energy for the exact solution. Eq. (2.8.5) is not energy-dependent, however, and as such the GCT equation seems to be in line with the theory. As the GCT makes use of the fact that $\nabla \cdot \mathbf{B} = 0$, and the applied spiral field is not divergence-free, there could be an energy-dependent effect from the magnetic potential induced by the magnetic field. This is possibly described by the analogous $\mathbf{v}_E$ described in section 4.2, which causes a drift in the $\hat{z}$-direction. As $\mathbf{v}_E$ describes the $\mathbf{E} \times \mathbf{B}$-drift (Cary and Brizard, 2009, Ch. III), the analogous magnetic potential would give

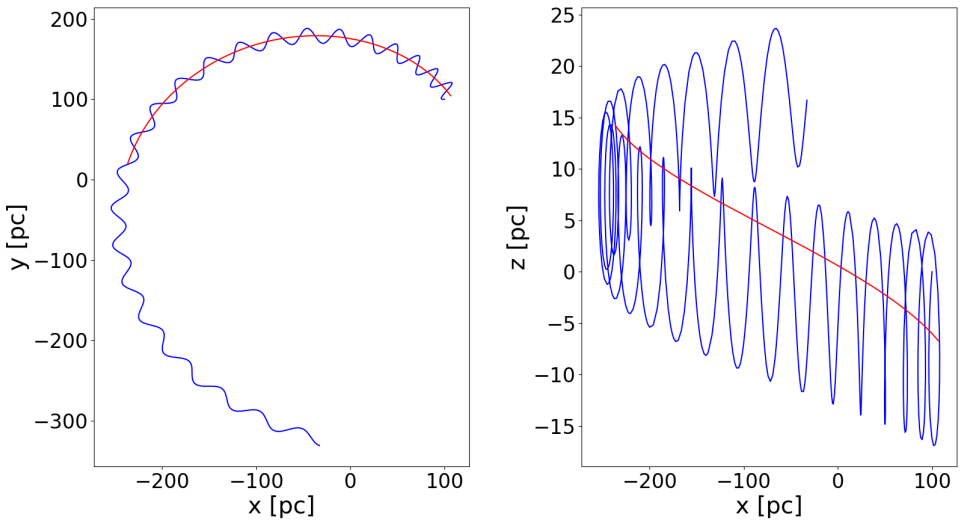

Figure 5.3: Simulation of a CR with an initial parallel velocity in the direction of the magnetic field line. The exact solution is plotted in blue, while the GCT solution is plotted in red. In this simulation the CR used was a proton with $E = 100\,\text{PeV}$.

rise to a field inducing its own drift velocity. As such the difference between the GC drift and exact solution drift in the discussed Figures could be attributed to the choice of a divergent magnetic field.

To test the effect of different ratios of energy to magnetic field strengths, the same simulation was done for ranges from $E = 1\,\mathrm{PeV}$ to $E = 1000\,\mathrm{PeV}$. The resulting trajectories for the two lowest energy CRs are shown in Figure A.4. Different initial velocities were also tested. All simulations gave equivalent results for all simulations, with the Larmor radius and $\hat{z}$-drift changing between the simulations. Two sample plots are given in Figure A.4, which were made using the same initial conditions as for Figure 5.3. As $v_{\parallel}$ is practically c for all the tested energies it is expected that trajectories are of equivalent lengths for both the GC solution and the exact solution. As seen, the plots show the trajectories being the same length.

5.2.3 Spiral Field with a Non-Constant Field Strength

After testing the GCT for both a uniform field and a spiral field with constant field strength, attempts were made to implement the GCT for a spiral field where the field strength was not constant. A factor depending on the angle and displacement of the CR was added to Eq. (5.2.3) as

$$\begin{aligned} \mathbf{B} &= B(\rho,\phi) \quad [\sin(\theta)\cos(\phi) - \cos(\theta)\sin(\phi)]\,\hat{x} \\ &+ B(\rho,\phi) \quad [\sin(\theta)\sin(\phi) + \cos(\theta)\cos(\phi)]\,\hat{y}. \end{aligned} \tag{5.2.4}$$

Inserting this into Eq. (5.1.4), the effective electric field would not be zero, as the magnetic field strength changes with respect to the spatial coordinates. In the implementation of the GCT the gradient effect should in theory be captured in the calculation of the effective electric field. As such, since the calculations of the effective electric field was found to return negligible values, this acceleration along the magnetic field line is missing. Furthermore, applying this field in the program led to the integrator being unable to calculate the trajectory. Immediately after starting the integration, Eq. (4.3.11) was determined to return values $\dot{u}\Delta t \gg c$, shortly after reaching $\dot{u} = \infty$.

One theory to explain this behavior was that the implemented equations are not relativistic. As such these equations, when directly applied with disregards to the relativistic limits, would allow for velocities greater than the speed of light. To account for this, the energy of the simulated CRs were tested for energies where $\gamma_L \sim 1$. This required the simulation time to be reduced as well. After tuning the simulations in the non-relativistic limit for the exact solution, the GCT simulations were tested. The same behavior still applied, with $\dot{u} \to \infty$ immediately. These results could be interpreted as showing the GCT is not working when an effective

electric field is introduced. However, a more likely explanation for this error is that the programming has not been done correctly, and there is still an error in the code used for the simulations. This error was shown to be confined to the part calculating the effective electric field, as the tests using magnetic fields without a gradient returned the expected result.

5.2.4 Uniform and Turbulent Fields in Superposition

Testing how the GCT performs when a turbulence is introduced was done by applying a turbulent magnetic field in superposition with the uniform field. From the assumptions made while deriving the EoM for the GC in Chapter 4, it is expected that the GCT achieves high accuracy when the turbulence is small compared to the uniform field.

Sample Trajectories

While the uniform fields in sections 5.2.1 and 5.2.2 were unable to generate an effective electric field, the turbulent magnetic field in general has $\nabla B \neq 0$. Thus, when a turbulence is applied, there should be an effective electric field accounting for gradient effects. Figure 5.4 shows the trajectory of one particle in a field with a turbulence $B_{\text{rms}} = 0.10 B_0$. As with the spiral field with constant field strength, the shape of the GC trajectory seems consistent with the trajectory of the exact solution. However, the exact solution is accelerated in different directions throughout the trajectory. Most notable is the acceleration in the z-direction compared to the GC trajectory. This acceleration for the exact solution is due to the gradient of the magnetic field induced by the turbulent part. As seen, a relatively small gradient can induce a significant acceleration to the CR. The expectancy of the simulation, when there is a gradient, is that the gradient effects would be captured by the GCT. However, the effective electric field was found to be negligible, with the largest values measured to $\mathbf{E}^* \sim 1 \cdot 10^{-20}\,\mathrm{V\,m^{-1}}$. From Figure A.5 it is apparent that perturbation as small as 1 % of the uniform field strength induces accelerations that are noticeable in the exact solution. Still, the GCT does not manage to capture these small acceleration effects. The same effect is apparent for all the tested ratios B_{rms}/B_0.

While the gradient effects that induce an acceleration is not apparent in the GCT, the shapes of the trajectories seem to be consistent with the exact solution. Figures 5.4 and A.5-A.8 show sample trajectories of CRs with $E = 100\,\mathrm{PeV}$, in magnetic fields where the turbulence ranges from 1 % to 100 % of the uniform magnetic field strength. Apart from missing drift-effects caused by the acceleration of the particles, the GC trajectories overlap well with the exact solution. In the case where the turbulence is 1 % of the uniform field strength there is almost no

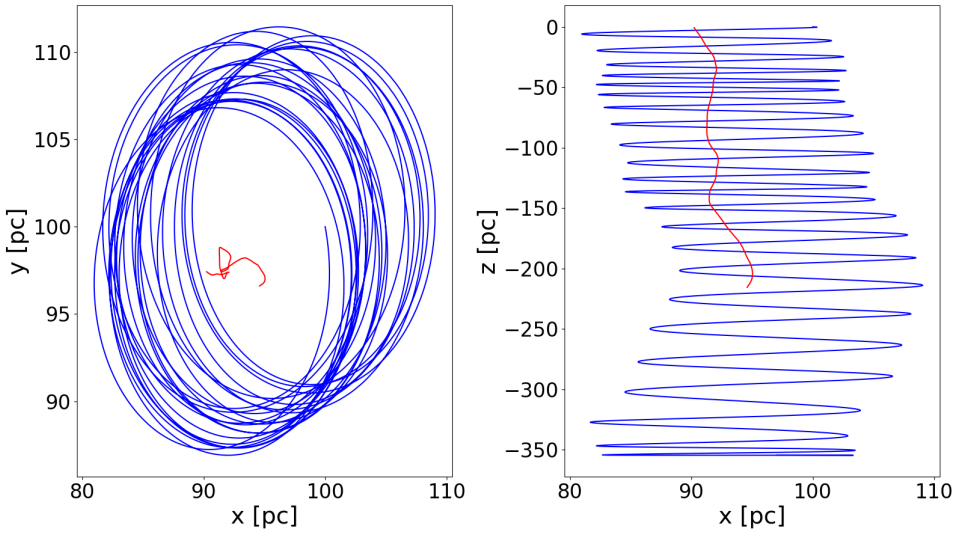

Figure 5.4: Simulation of a CR through a uniform magnetic field of strength $B_0 = 10\,\mu\text{G}$ in superposition with a turbulent magnetic field with $B_{\mathbf{RMS}} = 0.10\ B_0$. The exact solution is plotted as a blue line, while the GC is plotted as a red line.

drift in the x-direction, and the GC trajectory almost perfectly follows the center of the helical movement of the exact solution. When the turbulence is increased, more drift due to the gradient effects are induced. As such the GC trajectories do not follow the center of the exact solution. They do, however, still follow the same shaped path, which is clearly seen between $-150\,\text{pc}$ and $-200\,\text{pc}$ in the right panel of Figure 5.4. In Figure A.6, where the turbulence is 25 % of the uniform field strength, the GC lacks a lot of acceleration in the z-direction. However, the shape of the trajectory still looks identical to the exact solution for the distance the GC travels. The view of the xy-plane in the Figures for the two lowest percentages of turbulence do not provide a lot of information. When the turbulence is increased to 25 % it becomes more interesting, as there is now a significant amount of drift away from the original position in the xy-plane. The GC trajectory matches well with the exact solution, coarsely following the center of the helical movement. When the turbulence is increased to 50 %, in Figure A.7, the similarities between the trajectories become a bit more subtle in the xy-plane. Still, the projection onto the xz-plane show a high agreement between the shapes of the two trajectories. The majority of the GC trajectory follows alongside the exact trajectory, even when the exact trajectory show only small amounts of helical movement e.g. between $-200\,\text{pc}$ and $-300\,\text{pc}$ in the xz-plane. Following the trajectory in the xy-plane, there is seemingly a significant disagreement between the trajectories. Especially

in the lower-left corner of the Figure, the GC trajectory deviates from the exact solution. This part of the trajectory in the left panel of Figure A.7 coincides with the part in the right panel between $-200\,\mathrm{pc}$ and $-300\,\mathrm{pc}$. If the GC trajectory is carefully traced, it is found to follow coarsely the same pattern as the exact solution.

Lastly, the turbulence is set to be equal the uniform field strength, i.e $B_{\mathrm{rms}} = B_0$, as shown in Figure A.8. In this case the CR is quickly reflected, and the compared behavior between the GCT and the exact solution is in complete disagreement. Some other simulations were done, with other instances of the magnetic field, with the same results. At some point, not long after the beginning of the simulation, the particle would be reflected in the exact solution, and there was no way of comparing the trajectories any further.

The behavior of the sample trajectories, where the GC follows the same shape as the exact solution, points toward the GCT being able to produce trajectories that are in agreement with the exact solution, even when the gradient of the field becomes relatively large. However, the insignificant effective electric field is seemingly what hinders the GCT from being in proper agreement with the exact solution.

Statistical Comparison

As the representation of one single trajectory is heavily dependent on the instance of the magnetic field, these are not representative of the statistical value of the GCT. What is of interest is how accurate the GC simulations are relative to the exact solution, over a statistically significant amount of particles. Since the GC simulations proved to lack the gradient effect from the magnetic field, the method is expected to disagree with the exact solution when tested in magnetic fields with a gradient.

To test the statistical accuracy of the GCT, 1000 CRs were simulated for each ratio of B_{rms}/B_0 for energies in the range $1\,\mathrm{PeV}$ to $1000\,\mathrm{PeV}$. To measure the accuracy of the simulations the vector $\Delta\mathbf{r} = \mathbf{r}_{\mathrm{GCT}} - \mathbf{r}_{\mathrm{exact}}$ was first calculated, where the $\mathbf{r}$-vectors are the endpoints of the trajectories simulated by the GCT and exact solution respectively. For a perfect simulation using both methods, the distance between the endpoints should be exactly $1\,\mathrm{R_L}$. Using $|\Delta\mathbf{r}|/R_L$ as the measurement, a perfect simulation would give $|\Delta\mathbf{r}|/R_L = 1$. Averaging this measure over all 1000 CR trajectories then gives an idea of how accurate the GCT simulations are.

Figure 5.5 shows the results for all energies and B_{rms}/B_0-values. The most notable trend is that the accuracy of the GCT increases with energy. Looking at Eq. (3.1.1), this can be explained by the acceleration being inversely proportional to the energy of the CR. Due to the high energies the speed of the particles

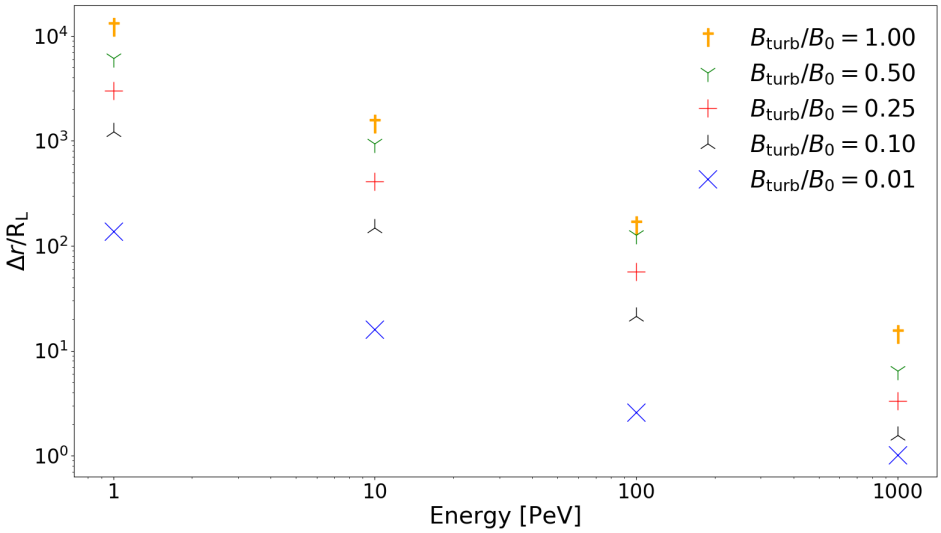

Figure 5.5: Average $\Delta r/R_L$ for energies in the range 1–10 PeV, and B_{rms}/B_0 values in the range 0.01–1.00. $\Delta r/R_L$ is plotted as a function of the energy.

is approximately constant and equal to c. At the same time γ_l increases and decreases with the same factor as the energy, i.e. $\gamma_l\,(10\,\text{PeV}) = 10\gamma_l\,(1\,\text{PeV})$. This leads to the acceleration increasing for lower energies. When the acceleration increases the turbulence will have a higher effect on the particle. This is explained by the relation between the correlation length of the turbulent magnetic field and the Larmor-radius of the CR. When the Larmor-radius is small compared to the correlation length, the CRs interact with more of the small-scale eddies of the turbulent magnetic field. Following this the local strength of the turbulence is increased relative to the uniform field. While the RMS of the turbulent field stays the same, the local variations become stronger and more apparent when the energy of the CR is lower.

Taking into account the lack of a gradient effect in the GCT, the behavior seen in Figure 5.5 is as expected with lower energies being less accurate overall. In Table B.1 the values of the points in Figure 5.5 are listed. Along with the Figure it can be concluded that the GCT is not accurate for energies below 1000 PeV for any amount of turbulence $\geq 0.01B_0$. The smallest value of $|\Delta\mathbf{r}|/R_L$ for these energies is 2.60 for 1 % turbulence and a particle with $E = 100\,\text{PeV}$. All other values are > 10, with most values being in excess of 100.

Looking at $E = 1000\,\text{PeV}$ the simulations are seemingly more accurate. For $B_{\text{rms}} = B_0$ the value of $|\Delta\mathbf{r}|/R_L = 14.4$, which is more accurate than for all amounts of turbulence for the lower energies, with the exception of 1 % turbulence

for $E = 100\,\mathrm{PeV}$. Lowering the percentage of turbulence to 10 %, the average deviation from the exact solution is $1.57\,\mathrm{R_L}$, while at 1 % is is only $1.01\,\mathrm{R_L}$. The GCT shows a high degree of accuracy for this energy, when the turbulence is low. However, at this energy the CR is well within the ballistic regime. This leads to the particle only interacting with the large scale eddies, mostly ignoring the effect of the small scale eddies. As such the turbulence affects the CR less in the ballistic regime. When the energy is at such a high level, and the RMS of the turbulence is set to 1 %, the turbulence is in practice negligible. Thus, it makes almost no difference if the turbulence is applied or not in the high-energy, low-B_{rms} case. At the same time it is important to note that increasing the turbulence with a factor 10, it is no longer negligible for $E = 1000\,\mathrm{PeV}$. At even higher energies, it would be expected that even higher percentages of B_{rms} would be negligible. Higher energies are seldom of interest, though, as CRs above 100 PeV will escape from the Galactic to the extragalactic regime.

To further investigate the behavior seen in Figure 5.5, the amount of particles with a distance $|\Delta\mathbf{r}|$ within different limits were counted. The results are shown in Tables 5.4 and B.2–B.4. From Table 5.4 the behavior when $E = 1000\,\mathrm{PeV}$ shown in Figure 5.5 is recognizable. For the low percentage of turbulence, a significant amount of particles are within $0.5\,\mathrm{R_L}$ of the exact solution. Furthermore, the majority of particles are found between $0.5\,\mathrm{R_L}$ and $2.5\,\mathrm{R_L}$. In this case only 3 particles are found to deviate in excess of $10\,\mathrm{R_L}$ from the exact solution. Again, this is explained by the low effect of the turbulence on the particles at such high energy. Most of the other Figures are approximately as expected with regards to Figure 5.5, with the majority of particles deviating in excess of $10\,\mathrm{R_L}$ compared to exact solution. One interesting case is in Table B.2, when the energy of the

Table 5.4: The amount of particles where the distance between the end point in the exact solution and the end point in the GC solution were within the given limits. The limits are offsets from $1\,\mathrm{R_L}$, meaning a particle at $\pm 0\,\mathrm{R_L}$ would be perfectly simulated relative to the exact solution. Each limit does not count the particles that were counted in the previous limit. Particles were counted for each of the different ratios of B_{RMS} and B_0. This table gives the values for simulations done for protons with energy 1000 PeV. Each of the 1000 particles were propagated in a different instance of the magnetic field.

B_{RMS}/B_0	$\pm 0.5\,\mathrm{R_L}$	$\pm 2.5\,\mathrm{R_L}$	$\pm 5.0\,\mathrm{R_L}$	$\pm 10.0\,\mathrm{R_L}$	$>10.0\,\mathrm{R_L}$
0.01	220	579	168	31	3
0.10	5	40	44	109	802
0.25	4	7	10	20	959
0.50	0	4	4	9	983
1.00	0	0	0	2	998

particle is $E = 1\,\mathrm{PeV}$ and the turbulence is $B_{\mathrm{rms}} = 0.01 B_0$. From Figure 5.5 the expectation is that the majority of particles would deviate from the exact solution by a factor of $\sim 100\,\mathrm{R_L}$. However, the particles are well spread between all the counted intervals. One possible explanation of this, is that the turbulence is at the threshold of being able to reflect particles. If a particle is reflected early on, in the exact solution it will travel a great distance in the opposite direction of the GC trajectory. However, if it is reflected late, or not at all, the GC trajectory will be closer to the exact solution. The same theory could also explain why there are more particles evenly spread over the intervals for the higher energies as well. Increasing the turbulence to $0.10\,\mathrm{R_L}$ immediately changes the distribution of the particles to almost all particles being in excess of $10\,\mathrm{R_L}$ from the exact solution. If the particles are more often reflected and accelerated abruptly perpendicular to $\hat{z}$, this will indeed make the GC deviate more from the exact solution.

5.2.5 Guiding-Center Simulation Efficiency

While the accuracy of the GCT is important in determining whether or not the method is useful, it is equally important whether or not it increases simulation efficiency. As the GCT is an approximation there is guaranteed to be some loss of information compared to the exact solution. The redemption for this is to gain a significant reduction in computation time.

For each of the particles simulated to create Figure 5.5, the runtime of both the exact and GC simulations were recorded. Using T for the runtime of the GC simulations and τ for the exact simulation, the proportional time spent on the simulations were calculated as T/τ and is shown in Figure 5.6. This is analogous to $|\Delta\mathbf{r}|/R_L$ in Figure 5.5. One important difference between the two Figures is that Figure 5.6 does not use a logarithmic scale for T/τ on the y-axis. It should also be noted that results are not ordered in Figure 5.6 as they are in Figure 5.5, but each simulation retains the same marker. Furthermore, the values of each point in Figure 5.6 is given in Table 5.5.

The first trend to notice, is that the GC simulation is more efficient relative to the exact solution for lower energies. The shape of the plot is similar to accuracies plotted in Figure 5.5, and as such it seems that the less accurate the GC simulations are, the more efficient they are. On the other hand the accuracy is always higher for smaller B_{rms}/B_0, while the average runtime is less for both larger and smaller B_{rms}/B_0.

For the smaller relative turbulence and higher energies the trajectory is practically just a helical movement along the $\hat{z}$-axis. As such the GC simulation only needs a fraction of the amount of points the exact calculation does to finish the trajectory. Due to the implementation of the GCT, it can simulate at most approximately 1/4 of the points of the exact solutions to be more efficient. In one

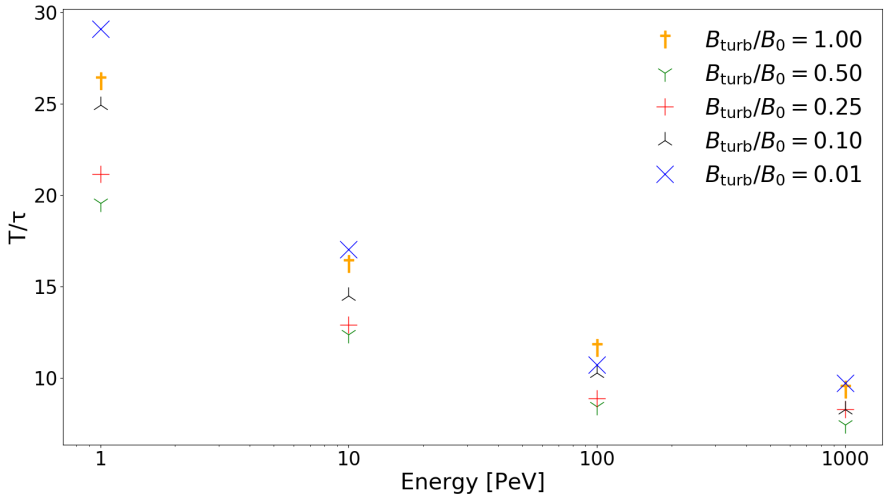

Figure 5.6: Average T/τ for energies in the range 1–10 PeV, and B_{rms}/B_0 values in the range 0.01–1.00. T/τ is plotted as a function of the energy.

step in the GC simulation, the turbulent field has to be calculated at least 4 times, while the exact solution only needs to calculate the magnetic field once for every step. The generation of the turbulence is by far the most time consuming part of the algorithm, leading to the approximate factor of 1/4 points to reach the same efficiency. Thus, in the uniform field and low-turbulence fields, where the trajectories are practically straight lines, the GC simulation can do with as little as $\sim 1/50$ of the points needed for the exact solution. During tests in the uniform field, the exact solution need just over 500 points, while the GC solution finished in 11-12 points. Introducing the smallest amount of turbulence, the exact solution needed about 1200-1500 points, while the GC needed around 100-200. Following this it seems reasonable that for high energies and small turbulences, the GC simulations are faster than the exact solution.

For small turbulences and low energies, however, the trajectories are no longer guaranteed to be close to the helical trajectories in the uniform field. Another possible explanation can be found by looking at Eqs. (5.1.5) and (5.1.4). Due to the low calculated values of $\mathbf{E}^*$, the second part of Eq. (4.3.12) becomes negligible when determining the accuracy in the integrator. This leads to $\mathbf{B}^*$ dominating the GC trajectory calculations. Since the magnetic field is modelled as a superposition between the uniform and the turbulent field, the effective field can also be written as

$$\mathbf{B}^* = \mathbf{B}^*_{\text{rms}} + \mathbf{B}_0, \tag{5.2.5}$$

where $\mathbf{B}^*_{\text{rms}}$ denotes the effective turbulent field and $\mathbf{B}_0$ is the uniform field. For

Table 5.5: The values of the average runtime difference T/τ, averaged over 1000 simulated CRs. The first column gives the ratio of turbulence to uniform field strength, while the other columns are the average T/τ values for the given energy. Here T is the runtime of the GC simulation, while τ is the runtime of the exact solution.

B_{RMS}/B_0	$E = 1\,\mathrm{PeV}$	$E = 10\,\mathrm{PeV}$	$E = 100\,\mathrm{PeV}$	$E = 1000\,\mathrm{PeV}$
0.01	29.10	17.02	10.70	9.71
0.10	24.93	14.48	10.28	8.29
0.25	21.16	12.92	8.88	8.28
0.50	19.56	12.38	8.43	7.43
1.00	26.25	16.25	11.65	9.36

the uniform field the effective field is equal to the real field, as there is no curl. While the turbulent field has a RMS value, it can deviate in strength up to several times the B_{rms}. This also means it can be several times weaker than the RMS value. As discussed in section 5.2.4 the turbulence becomes more prominent for lower energies.

From this it can then be explained why the small turbulence, low energy-case still has the highest efficiency. In this case the uniform field will still dominate the total magnetic field, and as such the helical movement must still be intact. Extending on this, the same must be true for all energies with a sufficiently large R_L compared to the scale size of the magnetohydrodynamic eddies modelling the turbulent magnetic field.

Looking at the rest of the points in Figure 5.6, the behavior of the runtime seems to roughly follow $T \propto (B_{\mathrm{rms}}/B_0)^2$. The simulations with $B_{\mathrm{rms}} = 0.50B_0$ have the lowest efficiency gain, while the simulations using $B_{\mathrm{rms}} = B_0$ are closer to the efficiency of the ones using $B_{\mathrm{rms}} = 0.01B_0$. In the simulations using $E = 100\,\mathrm{PeV}$ the $B_{\mathrm{rms}} = B_0$ case is actually more efficient than the $B_{\mathrm{rms}} = 0.01B_0$ case. As the turbulent magnetic field deviates from B_{rms} within the same order of magnitude, it becomes apparent that for the ratios of 10–50 %, the effective field is not dominated by either the uniform or turbulent field. For the 100 % case the turbulent field is able to dominate the uniform field.

Showing that the turbulent field is equal to or dominating the uniform field does not really affect the first part of Eq. (4.3.12). The first part in this equation, taking into account the Eq. (5.1.5), should still be correct with respect to the exact solution, whether the uniform or turbulent field is dominating. However, when the uniform field dominates, the effects from the gradient of the turbulent field, seen in Eq. (5.1.4), is negligible. When the turbulent field then becomes stronger relative to the uniform field, the gradient effect cannot be neglected. In the calculations it has been shown that the effective electric field was neglected for the GC simulations. For the cases where B_{rms} is 10–50 % of B_0, the gradient

effects are not dominant. In this range it is mainly $\mathbf{B}^*$ that controls the turbulent motion of the CR trajectory. As such the gradient effect, while not negligible, is still small enough to have less impact on the runtime of the calculations. When the turbulent field completely dominates the uniform field, however, the gradient effect is large enough to heavily impact the CR trajectory. At this point, since the GC simulation neglects this effect, the GC simulation disregards a major factor of the calculations, and following this the apparent efficiency increases. So while it seems there is an efficiency gain for higher relative turbulence, this is likely to be because the GCT fails to take into account the gradient effect.

While the GCT does not take into account the gradient effect of the field, it is important to note that the implementation does do the actual calculations needed. It only returns incorrect values. As such the gain in efficiency must not come from missing calculations, but rather the integrator not taking the gradient effects into account when calculating the error, and thus allowing for a larger error than the exact solution would.

Even though the GCT seems to be more efficient for higher turbulence, the explanation that the gradient effects is disregarded must be taken into account. At the same time, for higher turbulence, the GCT is expected to be less accurate. This also shown in Figure 5.5. Since the implementation of the GCT has not worked properly, it is still inconclusive whether or not it will be more efficient than the exact solution. Taking into account that the current GCT includes all the necessary computations, Figure 5.6 may give an idea of what to expect when it is properly implemented.

A last thing that has not been discussed, is the general efficiency over the different energies. As seen from the plot, the relative efficiency is lower for higher energies. This can be explained by a few different factors. First off, the particles with higher energies perpetrate more ballistic characteristics. As such they are not as heavily affected by the magnetic field, whether or not the turbulence dominates the field. At lower energies the particles are more diffusive, and are heavily affected by the magnetic field. When the particles are diffusive, the gradient effects become more prominent. For the lower-turbulence case, where the trajectories are still helical, the lower energy particles will also require higher accuracy in the exact solution, while the GC simulation will manage with only a few points to track the almost straight trajectory. As such the efficiency gain at lower energies will be large both when the turbulence and the uniform field dominates.

5.2.6 Known Errors and Future Development

In late development the insignificant effective electric field was found to be caused by an erroneous implementation of the units when calculating μ. After revealing this error in the program, the calculation of μ was fixed. This in turn led to

the integrator demanding a timestep on such a small scale that any meaningful simulations were rendered impossible. The program was set to abort for timesteps $\Delta t < 1 \cdot 10^{-4}$ s, and the attempts made to redeem this error were unsuccessful.

At the end of development of the program there were still several issues. For different parameters and magnetic fields the performance of the GCT would vary enourmously, depending on for example if there was a turbulence in a uniform field, turbulence in a spiral field or simply a uniform or spiral field. However, most of the errors seemed to be connected to incorrect units or numerical errors. With the results seen from the GCT in this chapter, it gives an indication that the theory will provide a statistically robust method, even for magnetic fields that changes abruptly over the spatial coordinates. Fixing the error in how the units are calculated should result in the expected effects from the curl and the gradient of the field, to become apparent. When the behavior of the GCT is as expected, the numerical errors leading to slow integrations can be rectified.

If the behavior of the GCT were to be fixed, optimization of the algorithm could be performed. There are two obvious possible weak points in the program as it stands. The first one is the choice of the integrator. As most tests done for this report were done using non-turbulent fields, either by themselves or in superposition with turbulent fields, the Bulirsch-Stoer integrator was chosen. This is an integrator that has its strengths when the functions are smooth. As such there are better choices for the integrator in fields that change abruptly, as the turbulent fields do.

The second possible weak spot in the calculation are the derivatives used when calculating the effective fields. First off, the magnetic field, including turbulence, is calculated four times in the current program. In comparison, the exact solution only generates the magnetic field once for every four times the GCT generates the field.

Furthermore, the spatial derivatives of the magnetic field were calculated using a first order forward differentiation scheme. The timestep used was generated taking the time step of a full step for the integrator, multiplying it with the current GC velocity. As such, both a more accurate and more effective method should be possible to apply. The accuracy of the effective electric field will depend heavily on the accuracy of these derivatives, so it will be imperative to properly develop this part of the algorithm.

CHAPTER 6

CONCLUSION

The aim of this project was to apply Hamiltonian GCT to the propagation of CR through the Galactic magnetic field, and test under which conditions this method could be expected to produce statistically useful results. As such, the diffusion of CR through a turbulent magnetic field was investigated, to both test the isotropy of the method used to generate the turbulent field, as well as to prepare a method that could compare the results of the Hamiltonian GCT to those of the exact solution. After this the Hamiltonian GCT was applied to the propagation of CR. However, the development of the program implementing the Hamiltonian GCT faced several difficulties, and in the end there was not enough time to apply it to the diffusion through the turbulent magnetic field. Presented here are then the conclusion of the chapter on diffusion of CR through the turbulent magnetic field, followed by the conclusion on the implementation of the Hamiltonian GCT.

Diffusion of Cosmic Rays in a Turbulent Magnetic Field

The aim of investigating the diffusion of CR in a turbulent magnetic field was twofold. Giacalone and Jokipii (1994) present a method of generating a turbulent magnetic field, which Tautz (2012) claims is not isotropic. As an isotropic turbulent field is needed to properly simulate the diffusion of CR in the Galactic magnetic field, this isotropy had to be investigated. Furthermore, if the generated turbulent field was indeed isotropic, the diffusion of CRs would be a good method to test how well the Hamiltonian Guiding Center compares to the simulations using the exact solution of the Lorentz force.

The first step to find whether or not the turbulent magnetic field is isotropic, was to analytically check the algorithm. In section 2.5 the calculations are shown. The field is found to be analytically isotropic under the assumptions that the

number of Fourier modes n_k used is sufficiently large, and that the particles are propagated a distance such that $k_j|z'|_{max} \gg 2\pi$. Furthermore, isotropy is only achieved by choosing a proper set of probability distribution, which are given in table 2.1.

From the simulations of particles propagating in different turbulent magnetic fields, the diffusion coefficients were calculated and plotted as a function of time. The coefficients were found to behave as expected when compared to the results in Giacinti et al. (2012). For the turbulent magnetic field a $B_{\rm rms}$ value of $4\,\mu$G was used. With $L_{\rm max} = 150\,$pc the anisotropic behavior of diverging diffusion coefficients was found to start after a few years for $E = 1\,$PeV, with the behavior starting later for higher energies.

The behavior of the diffusion was shown to be anisotropic in the limit where $|\mathbf{r}| \lesssim$ a few L_c. Intensity plots of the diffusion, shown in Figures 3.6–A.2, clearly show the expected filamentary structures in this limit.

In the isotropic limit $|\mathbf{r}| \gg L_c$ the diffusion coefficients converged to a certain degree. The factor d_3/d_1, used as a measure of anisotropy, was found to be approximately constant at $d_3/d_1 \sim 10$ for all simulations. This is in agreement with Giacinti et al. (2012) when $E = 1\,$PeV. However, in Giacinti et al. (2012) d_3/d_1 seems to be inversely proportional to the energy. Possible errors were discussed, with numerical errors seemingly being the major contributor to this anisotropic behavior in the isotropic regime.

Comparing the calculated average diffusion coefficients to the expected value given by the diffusion functional in Eq. (2.10.4), the behavior of the simulated diffusion coefficients is found to be in agreement with that of the theoretical coefficients. However, the transition is found to happen at slightly higher energy levels in the simulations, compared to what is calculated using the diffusion functional. At the same time the amplitude of the diffusion coefficients is found to be in agreement with the theoretical coefficients. The deviation between the theoretical and simulated diffusion coefficients were found to be between a factor of 1.21 and 2.33.

In conclusion the expected behavior of the diffusion of CRs in a turbulent magnetic field has been qualitatively shown. The diffusion behaves as expected in the anisotropic regime, while in the isotropic regime there is a small factor of anisotropy that is not expected. This factor of anisotropy in the isotropic regime is most likely due to numerical inaccuracy in the simulations. Furthermore, the magnitude of the diffusion coefficients is found to be in agreement with the expected values. The results of Giacinti et al. (2012) and Giacinti et al. (2018) have been sufficiently reproduced. The program has been shown to be of sufficient quality to be used to test under which conditions the Hamiltonian GCT is accurate.

Hamiltonian Guiding Center Theory

The Hamiltonian GCT was applied to cosmic ray propagation through the Galactic magnetic field with partial success. Following the derivation of the theory from Cary and Brizard (2009), the equations of motion were implemented using a Runge-Kutta method provided by Press et al. (2007).

For the simple case of a uniform field the GCT was shown to simulated the trajectory of the particle perfectly. When a curl was applied to the field, the simulations proved to be able to simulate the expected trajectory, including the drift effect induced by the curl of the field.

When attempting to simulate cosmic ray propagation through a spiral field with a non-constant field strength, the simulations broke down, and the integrator was unable to simulate the trajectory for the guiding center.

Applying the GCT to the propagation of CRs through a uniform field in superposition with a turbulent field, the guiding center simulation followed the same shape as the exact solution, but it lacked some of the drift and acceleration effects. The drift effects were found to be missing due to an erroneous unit calculation, but it was not possible within the timeframe of the project to correct this error. The missing drift effect was also shown to be caused by a different error due to by improper implementation of units.

The GCTwas shown to be inaccurate compared to the exact solution when applied to 1000 particles propagated in different magnetic fields consisting of a uniform part in superposition with a turbulent part. For higher energies the accuracy increased, due to the trajectory approaching that of the trajectory in a uniform field. The GCT was also shown to be less accurate the higher the RMS value to the turbulent field was with respect to the uniform field strength.

Comparing the efficiency of the GCT to that of the exact solution, it was shown to be more efficient, with the efficiency increasing for lower energies. Furthermore, the efficiency was at the lowest when the RMS of the turbulence was 50 % of the uniform field strength. The efficiency increase both for increasing and decreasing values of B_{RMS}. While the efficiency increased with lower energy for the GCT, the accuracy decreased.

In conclusion the Hamiltonian GCT seems to behave in accordance with the exact solution. If the errors in the implementations were to be fixed, it would be expected that the accuracy increases drastically for all the tested configurations of the magnetic field. At the same time it would be expected that efficiency of the GCT stabilizes as the accuracy increases, while still maintaining a significant efficiency gain compared to the exact solution.

BIBLIOGRAPHY

K. J. Andersen. Charged Particle Motion in Turbulent Magnetic Fields. *NTNU*, 2017.

R. Beck. Magnetic fields in the Milky Way and other spiral galaxies. *ArXiv Astrophysics e-prints*, October 2003.

Rainer Beck and Richard Wielebinski. Magnetic Fields in the Milky Way and in Galaxies, 2013.

Allen H Boozer. Guiding center drift equations. *The Physics of Fluids*, 23(5):904–908, 1980.

François Boulanger et al. IMAGINE: A comprehensive view of the interstellar medium, Galactic magnetic fields and cosmic rays. *JCAP*, 1808(08):049, 2018. doi: 10.1088/1475-7516/2018/08/049.

John R. Cary and Alain J. Brizard. Hamiltonian theory of guiding-center motion. *Rev. Mod. Phys.*, 81:693–738, May 2009. doi: 10.1103/RevModPhys.81.693. URL `https://link.aps.org/doi/10.1103/RevModPhys.81.693`.

J. Giacalone and J. R. Jokipii. Charged-particle motion in multidimensional magnetic-field turbulence. *Astrophysical Journal Letters*, 430:L137–L140, August 1994. doi: 10.1086/187457.

G. Giacinti, M. Kachelriess, and D. V. Semikoz. Filamentary Diffusion of Cosmic Rays on Small Scales. *Phys. Rev. Lett.*, 108:261101, 2012. doi: 10.1103/PhysRevLett.108.261101.

G. Giacinti, M. Kachelriess, and D. V. Semikoz. Reconciling cosmic ray diffusion with Galactic magnetic field models. *JCAP*, 1807(07):051, 2018. doi: 10.1088/1475-7516/2018/07/051.

David J Griffiths. *Introduction to electrodynamics; 4th ed.* Pearson, Boston, MA, 2013. doi: 1108420419. URL `https://cds.cern.ch/record/1492149`. Re-published by Cambridge University Press in 2017.

Diego Harari, Silvia Mollerach, Esteban Roulet, and Federico Sanchez. Lensing of ultrahigh-energy cosmic rays in turbulent magnetic fields. *JHEP*, 03:045, 2002. doi: 10.1088/1126-6708/2002/03/045.

Marijke Haverkorn. Magnetic Fields in the Milky Way, 2014.

Marijke Haverkorn et al. Measuring magnetism in the Milky Way with the Square Kilometre Array. *PoS*, AASKA14:096, 2015. doi: 10.22323/1.215.0096.

L.D. Landau and E. M. Lifshitz. *The Classical Theory of Fields.* Pergamon Press, 1971.

Robert G. Littlejohn. Variational principles of guiding centre motion. *Journal of Plasma Physics*, 29(1):111–125, 1983. doi: 10.1017/S002237780000060X.

Theodore G Northrop. Adiabatic charged-particle motion. *Reviews of Geophysics*, 1(3): 283–304, 1963.

William H. Press, Saul A. Teukolsky, William T. Vetterling, and Brian P. Flannery. *Numerical Recipes in C++.* Cambridge University Press, Cambridge, USA, third edition, 2007.

David Ruelle. A theory of hydrodynamic turbulence based on non-equilibrium statistical mechanics. *Journal of Statistical Physics*, 169(6):1039–1044, Dec 2017. ISSN 1572-9613. doi: 10.1007/s10955-017-1914-8. URL `https://doi.org/10.1007/s10955-017-1914-8`.

Yakov M Shnir. *Magnetic monopoles.* Springer Science & Business Media, 2006.

A. P. Snodin, A. Shukurov, G. R. Sarson, P. J. Bushby, and L. F. S. Rodrigues. Global diffusion of cosmic rays in random magnetic fields. *Mon. Not. Roy. Astron. Soc.*, 457 (4):3975–3987, 2016. doi: 10.1093/mnras/stw217.

Prachanda Subedi et al. Charged particle diffusion in isotropic random magnetic fields. *Astrophys. J.*, 837(2):140, 2017. doi: 10.3847/1538-4357/aa603a.

R. C. Tautz. On Simplified Numerical Turbulence Models in Test-particle Simulations. *J. Comput. Phys.*, 231:4537–4541, 2012. doi: 10.1016/j.jcp.2012.02.021.

RB White, Allen H Boozer, and Ralph Hay. Drift hamiltonian in magnetic coordinates. Technical report, Princeton Univ., 1982.

H Vernon Wong. Hamiltonian formulation of guiding center motion and of the linear and nonlinear gyrokinetic equation. *The Physics of Fluids*, 25(10):1811–1820, 1982.

ACRONYMS

CR Cosmic Rays.

EoM Equations of Motion.

GC Guiding Center.

GCT Guiding Center Theory.

ODE Ordinary Differential Equation.

RK Runge-Kutta.

RMS Root Mean Square.

RNG Random Number Generator.

TMF Turbulent Magnetic Field.

Appendices

APPENDIX A

ADDITIONAL FIGURES

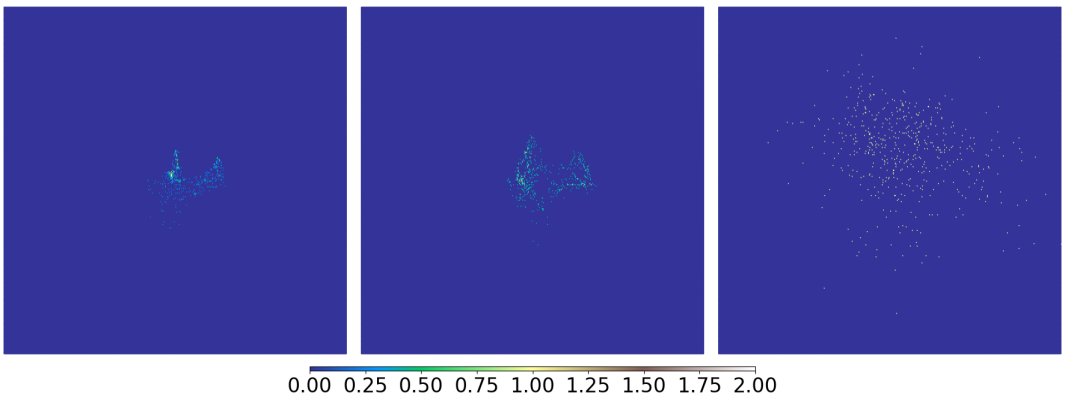

Figure A.1: Intensity plot of 1000 protons' position projected onto the xy-plane. A brighter color means more particles are projected onto that area. In this plot $E = 1\,\text{PeV}$ and $L_{\text{max}} = 10\,\text{pc}$. The positions are recorded, from left to right, at times $t = 8\,\text{years}$, $t = 10\,\text{years}$ and $t = 50\,\text{years}$, to show how the diffusion develops over time. The x and y axes are in parsec, and are scaled with respect to the furthest propagated particles in each direction.

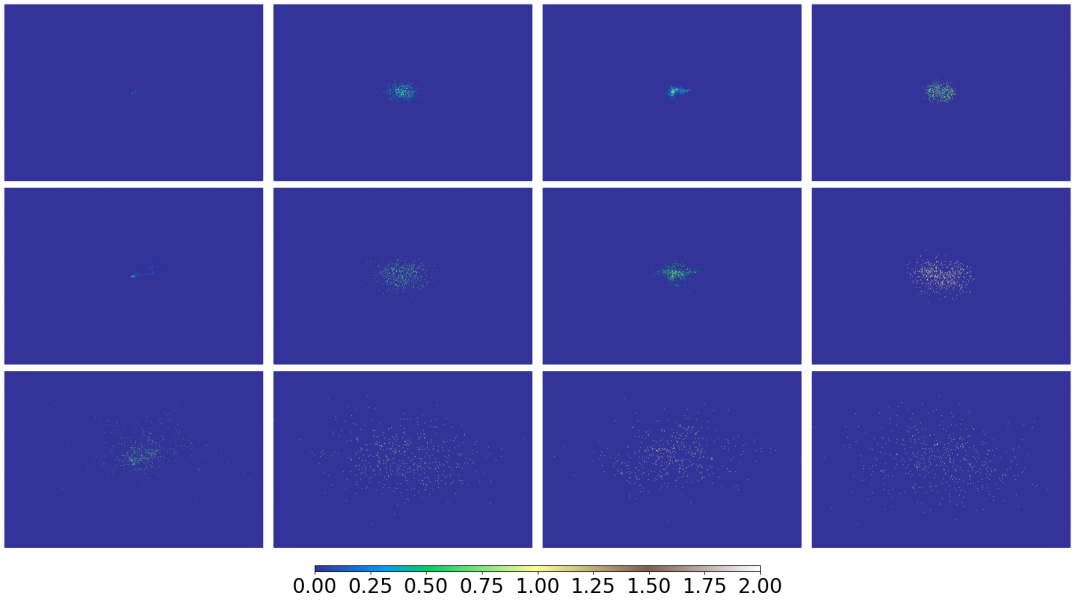

Figure A.2: Comparison of the intensity plots of the two lowest energies simulated. The proton positions are recorded at $t = 500\,\text{years}$, $t = 1000\,\text{years}$ and $t = 7000\,\text{years}$, with time increasing for each row. A brighter color indicates more particles were projected onto that area of the xy-plane. The two left columns have energy $E = 1\,\text{PeV}$, while the two rightmost columns have $E = 10\,\text{PeV}$. The first column for each energy has $L_{\text{max}} = 150\,\text{pc}$, and the second has $L_{\text{max}} = 10\,\text{pc}$. The x- and y-axes are in parsecs, and are scaled with respect to the furthest propagated particles in each direction.

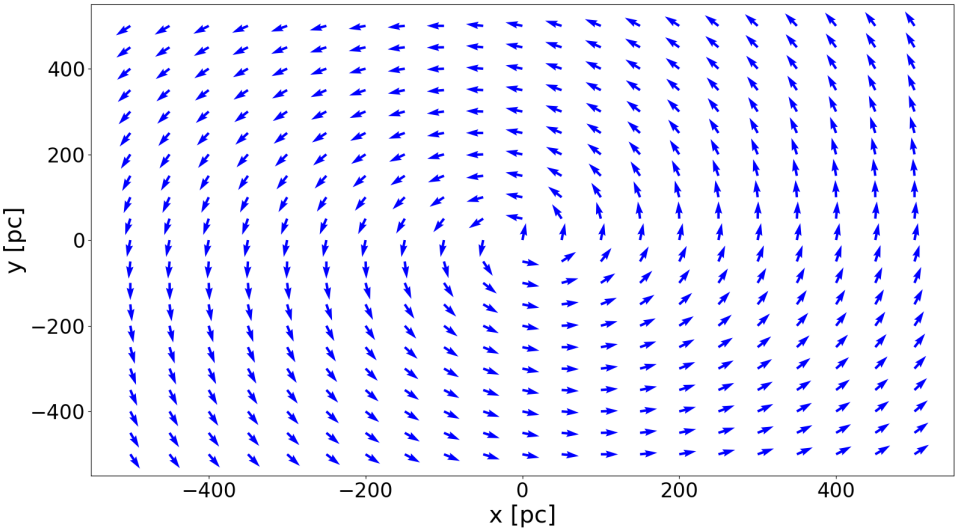

Figure A.3: Visual representation of the spiral field generated by Eq. (5.2.3). Arrows are plotted every 50 pc in a 1000 pc × 1000 pc plane centered around $(x, y) = (0, 0)$.

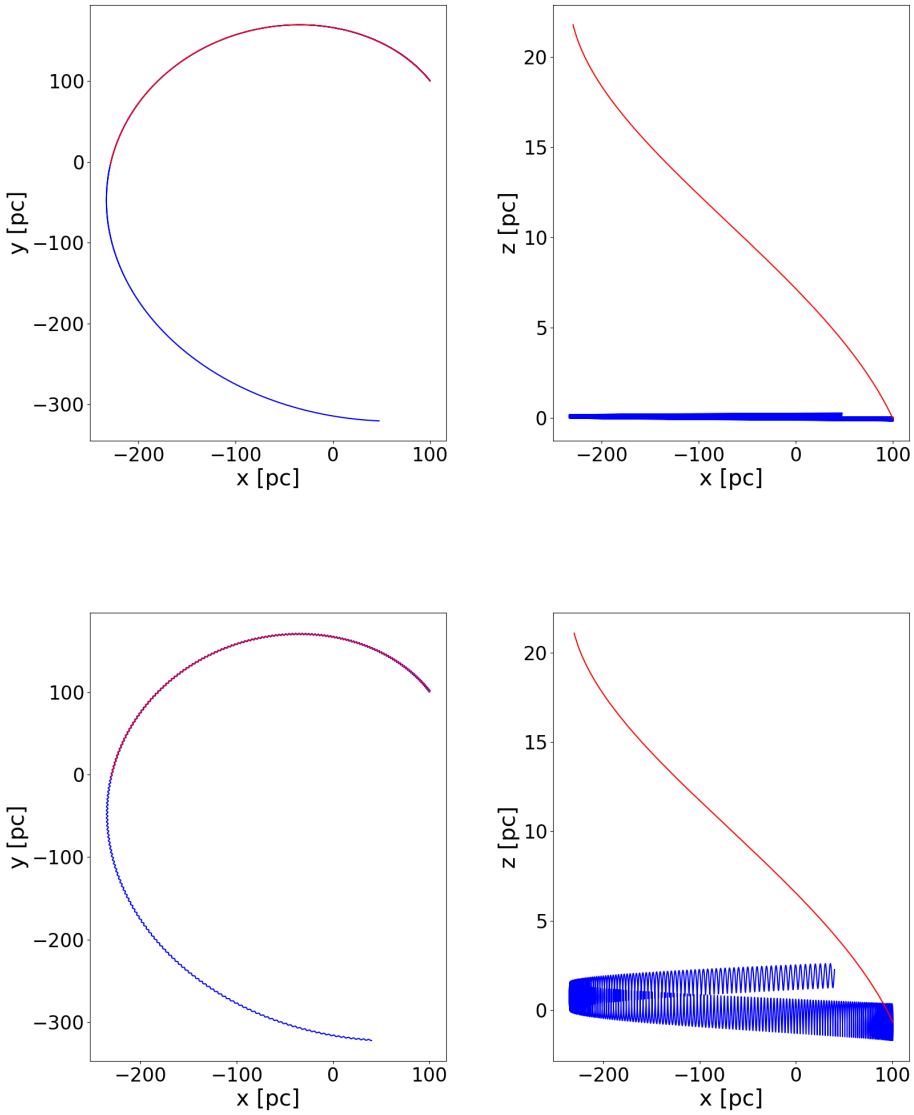

Figure A.4: Simulation of two CRs with an initial parallel velocity in the direction of the magnetic field line. The exact solution is plotted in blue, while the GCT solution is plotted in red. In the upper simulation the CR used was a proton with $E = 1\,\mathrm{PeV}$, while for the lower simulation a proton with $E = 10\,\mathrm{PeV}$ was used.

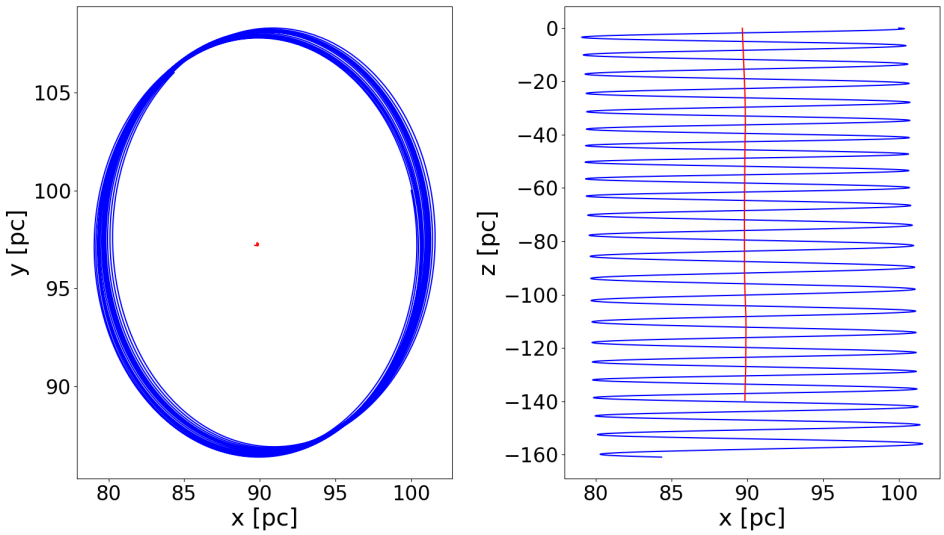

Figure A.5: Simulation of a CR through a uniform magnetic field of strength $B_0 = 10\,\mu\text{G}$ in superposition with a turbulent magnetic field with $B_{\text{rms}} = 0.01\ B_0$. The exact solution is plotted as a blue line, while the GC is plotted as a red line.

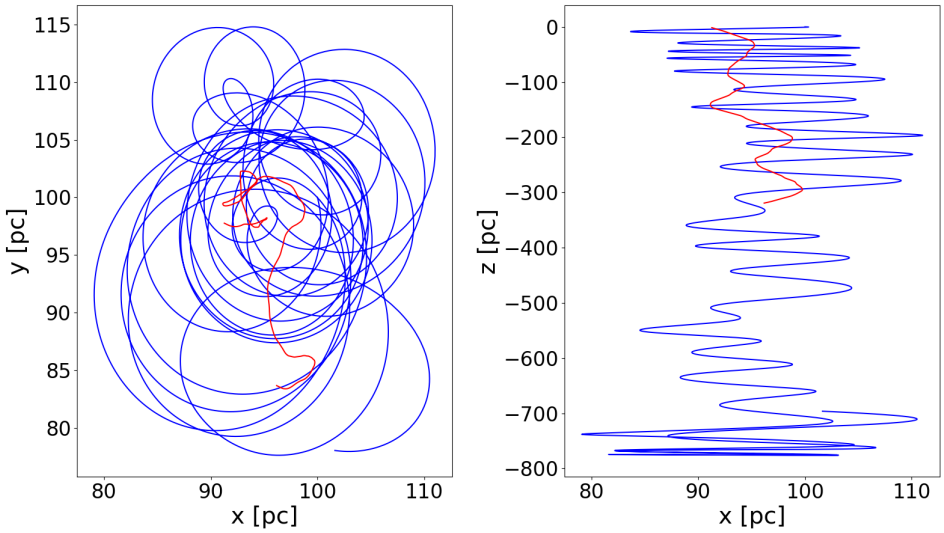

Figure A.6: Simulation of a CR through a uniform magnetic field of strength $B_0 = 10\,\mu\text{G}$ in superposition with a turbulent magnetic field with $B_{\mathbf{rms}} = 0.25\ B_0$. The exact solution is plotted as a blue line, while the GC is plotted as a red line.

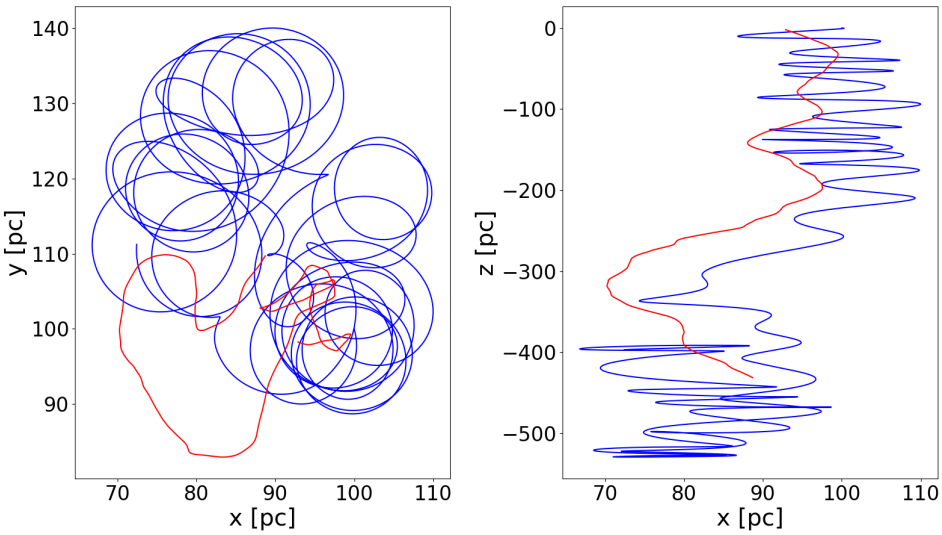

Figure A.7: Simulation of a CR through a uniform magnetic field of strength $B_0 = 10\,\mu\text{G}$ in superposition with a turbulent magnetic field with $B_{\mathbf{RMS}} = 0.50\ B_0$. The exact solution is plotted as a blue line, while the GC is plotted as a red line.

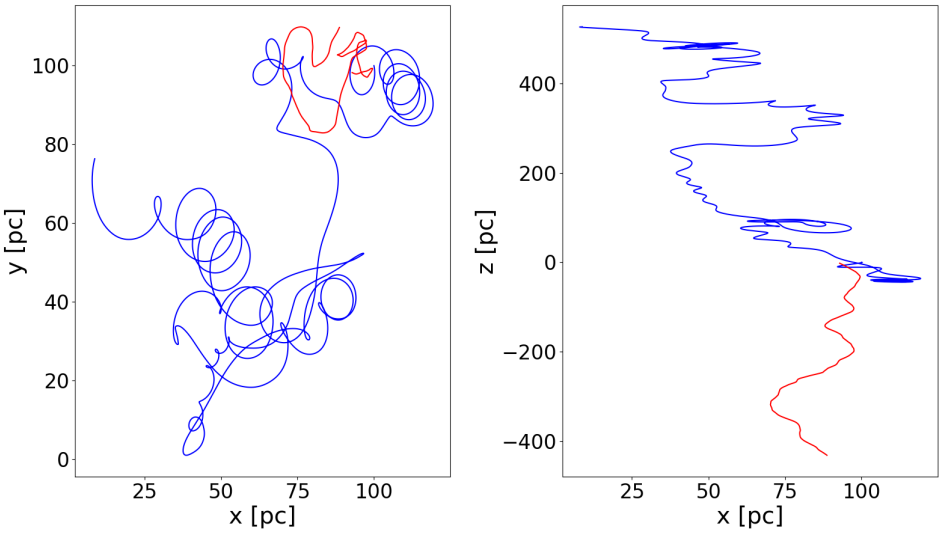

Figure A.8: Simulation of a CR through a uniform magnetic field of strength $B_0 = 10\,\mu\text{G}$ in superposition with a turbulent magnetic field with $B_{\mathbf{rms}} = 1.00\ B_0$. The exact solution is plotted as a blue line, while the GC is plotted as a red line.

APPENDIX B

ADDITIONAL TABLES

Table B.1: The values of the calculated $|\Delta\mathbf{r}|/R_L$, averaged over 1000 simulated CRs. The first column gives the ratio of turbulence to uniform field strength, while the other columns are the average $|\Delta\mathbf{r}|/R_L$ values for the given energy.

B_{RMS}/B_0	$E = 1\,\mathrm{PeV}$	$E = 10\,\mathrm{PeV}$	$E = 100\,\mathrm{PeV}$	$E = 1000\,\mathrm{PeV}$
0.01	$1.38 \cdot 10^2$	$1.60 \cdot 10^1$	2.60	1.01
0.10	$1.22 \cdot 10^3$	$1.49 \cdot 10^2$	$2.13 \cdot 10^1$	1.57
0.25	$3.01 \cdot 10^3$	$4.08 \cdot 10^2$	$5.69 \cdot 10^1$	3.31
0.50	$6.16 \cdot 10^3$	$9.41 \cdot 10^2$	$1.27 \cdot 10^2$	6.42
1.00	$1.22 \cdot 10^4$	$1.46 \cdot 10^3$	$1.56 \cdot 10^2$	$1.44 \cdot 10^1$

Table B.2: The amount of particles where the distance between the end point in the exact solution and the end point in the GC solution were within the given limits. The limits are offsets from $1\,\mathrm{R_L}$, meaning a particle at $\pm 0\,\mathrm{R_L}$ would be perfectly simulated relative to the exact solution. Each limit does not count the particles that were counted in the previous limit. Particles were counted for each of the different ratios of B_{RMS} and B_0. This table gives the values for simulations done for protons with energy 1 PeV. Each of the 1000 particles were propagated in a different instance of the magnetic field.

B_{RMS}/B_0	$\pm 0.5\,\mathrm{R_L}$	$\pm 2.5\,\mathrm{R_L}$	$\pm 5.0\,\mathrm{R_L}$	$\pm 10.0\,\mathrm{R_L}$	$>10.0\,\mathrm{R_L}$
0.01	117	225	188	159	311
0.10	6	29	33	58	874
0.25	1	6	18	26	949
0.50	0	4	5	8	983
1.00	0	2	0	5	993

Table B.3: The amount of particles where the distance between the end point in the exact solution and the end point in the GC solution were within the given limits. The limits are offsets from 1 R_L, meaning a particle at $\pm 0\,R_L$ would be perfectly simulated relative to the exact solution. Each limit does not count the particles that were counted in the previous limit. Particles were counted for each of the different ratios of B_{RMS} and B_0. This table gives the values for simulations done for protons with energy 10 PeV. Each of the 1000 particles were propagated in a different instance of the magnetic field.

B_{RMS}/B_0	$\pm 0.5\,R_L$	$\pm 2.5\,R_L$	$\pm 5.0\,R_L$	$\pm 10.0\,R_L$	$>10.0\,R_L$
0.01	117	217	152	163	351
0.10	6	16	16	44	918
0.25	1	1	11	16	971
0.50	0	1	1	8	991
1.00	0	0	0	2	998

Table B.4: The amount of particles where the distance between the end point in the exact solution and the end point in the GC solution were within the given limits. The limits are offsets from 1 R_L, meaning a particle at $\pm 0\,R_L$ would be perfectly simulated relative to the exact solution. Each limit does not count the particles that were counted in the previous limit. Particles were counted for each of the different ratios of B_{RMS} and B_0. This table gives the values for simulations done for protons with energy 100 PeV. Each of the 1000 particles were propagated in a different instance of the magnetic field.

B_{RMS}/B_0	$\pm 0.5\,R_L$	$\pm 2.5\,R_L$	$\pm 5.0\,R_L$	$\pm 10.0\,R_L$	$>10.0\,R_L$
0.01	107	222	142	178	351
0.10	2	16	15	35	932
0.25	0	1	0	6	993
0.50	0	0	0	0	1000
1.00	0	0	0	0	1000

APPENDIX C

EXTERNAL FIGURES

A selection of figures from Giacinti et al. (2012) and Giacinti et al. (2018) are appended here for easier comparison to the results presented in this report. The original captions are added as part of the figures, with new captions below these. It is the last captions that give the figure numbers for the placement in this report.

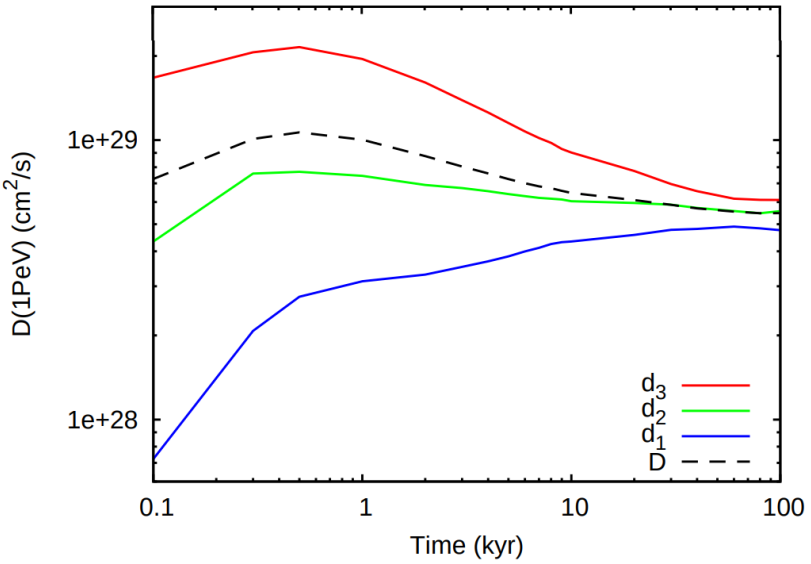

FIG. 1: Eigenvalues d_i (solid lines) of the diffusion tensor $D_{ij} = \langle x_i x_j \rangle / (2t)$ together with the average diffusion coefficient D (dashed line) as function of time t. For $B_{\rm rms} = 4\,\mu$G, $l_{\rm max} = 150\,$pc, $\alpha = 5/3$ and CR energy $E = 10^{15}\,$eV.

Figure C.1: Figure 1 from Giacinti et al. (2012)

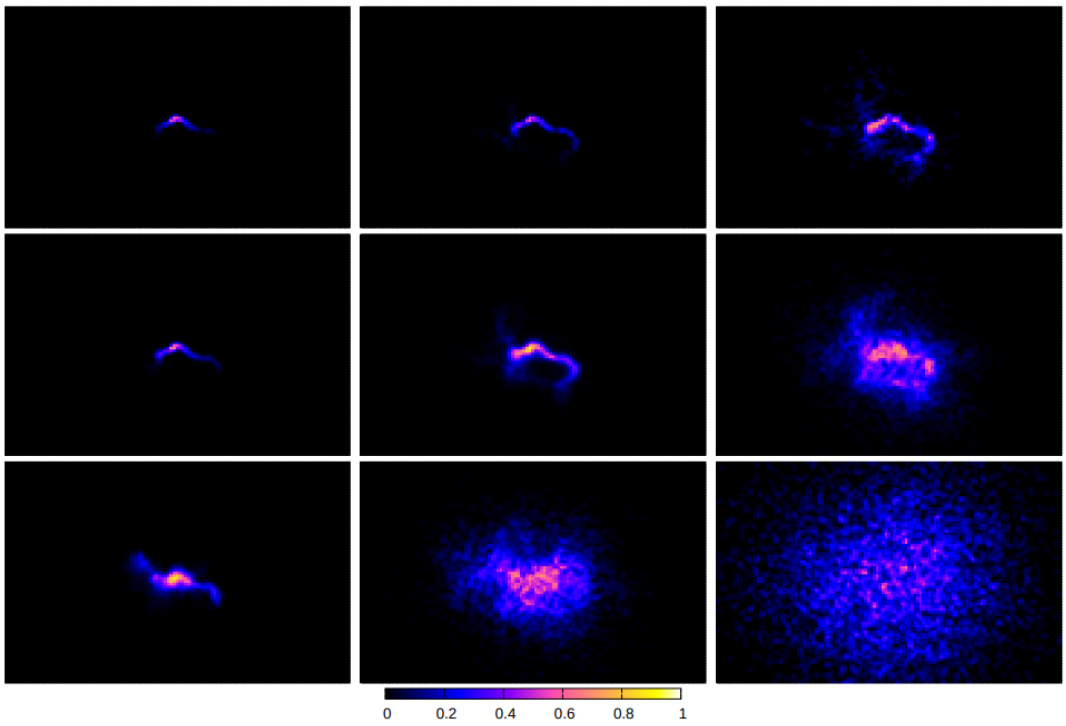

FIG. 2: Relative cosmic ray densities around their source projected in the panel planes, for energies $E = 100\,\mathrm{TeV}$ *(upper row)*, $1\,\mathrm{PeV}$ *(middle row)*, $10\,\mathrm{PeV}$ *(lower row)* and times $t = 500\,\mathrm{yr}$ *(left column)*, $2\,\mathrm{kyr}$ *(middle column)*, $7\,\mathrm{kyr}$ *(right column)*. Same field realization in each panel. Each panel corresponds to a $600\,\mathrm{pc} \times 400\,\mathrm{pc}$ field-of-view, with the source located in the center.

Figure C.2: Figure 2 from Giacinti et al. (2012)

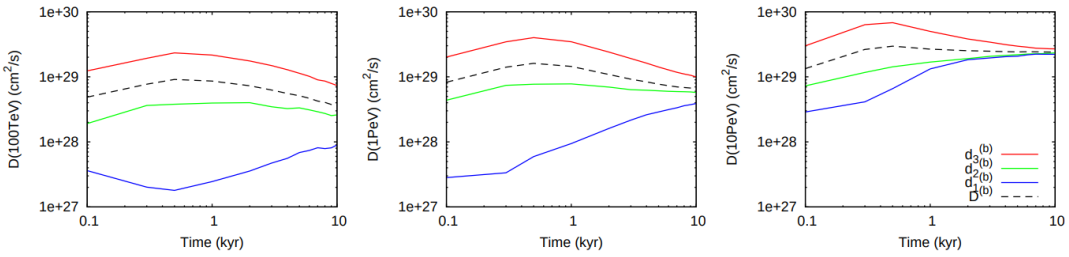

FIG. 3: Eigenvalues $d_i^{(b)}$ of the diffusion tensor D_{ij} as function of time t for energies $E = 100\,\mathrm{TeV}$ *(left)*, $1\,\mathrm{PeV}$ *(middle)* and $10\,\mathrm{PeV}$ *(right)*. Same field realization as in Fig. 2. Dashed lines for the average diffusion coefficient $D^{(b)} \simeq D$.

Figure C.3: Figure 3 from Giacinti et al. (2012)

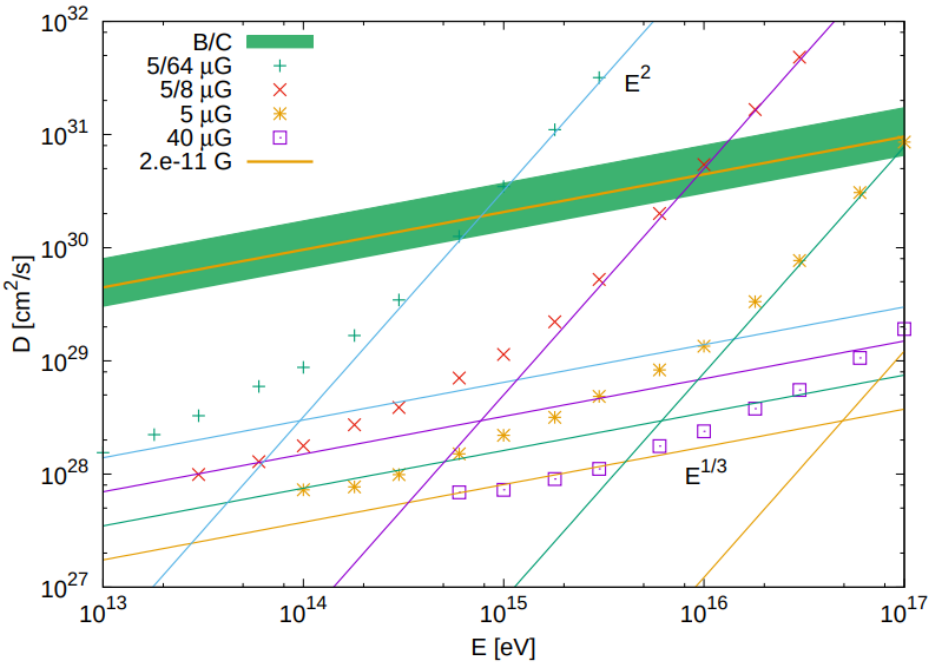

Figure 1. CR diffusion coefficient in pure isotropic Kolmogorov turbulence with $L_{\rm max} = 25\,{\rm pc}$ and for four values of the turbulence root-mean-square strength: $B_{\rm rms} = 40\,\mu{\rm G}$, $5\,\mu{\rm G}$, $(5/8)\,\mu{\rm G}$, and $(5/64)\,\mu{\rm G}$ —see key for symbols. The asymptotic behaviours at low and high energies are shown with the solid lines. The lines $\propto E^{1/3}$ differ by a factor $8^{1/3} = 2$ in normalization. We also plot, in orange, the extrapolated asymptotic low-energy behaviour for $B_{\rm rms} = 2 \times 10^{-5}\,\mu{\rm G}$. It lies within the range of magnetic field strengths that satisfy $D_0 = (3-8) \times 10^{28}{\rm cm}^2/{\rm s}$ at $E_0 = 10\,{\rm GeV}$, assuming a "Kolmogorov" extrapolation to high energies (B/C constraints from Refs. [1, 2], green area).

Figure C.4: Figure 1 from Giacinti et al. (2018)